UNIVERSITAT POLITÈCNICA DE CATALUNYA
BARCELONATECH
E scola Tècnica Superior d'Enginyeria
de Telecomunicació de Barcelona

Preparation and manipulation of free-standing oxides for photovoltaic applications

A Master's Thesis
Submitted to the Faculty of the
Escola Tècnica d'Enginyeria de Telecomunicació de Barcelona
Universitat Politècnica de Catalunya
by
Ivan Caño Prades

In partial fulfilment
of the requirements for the degree of
PHYSICS ENGINEERING

Supervisor: Mariona Coll Bau
Tutor: Pol Lloveras Muntané

Barcelona, July 17, 2020

UNIVERSITAT POLITÈCNICA DE CATALUNYA BARCELONATECH

telecos BCN

Title of the thesis: Preparation and manipulation of free-standing oxides for photovoltaic applications

Author: Ivan Caño Prades

Supervisor: Mariona Coll Bau

Abstract

Epitaxial complex oxides are of great interest for their rich chemical and physical properties, and their functionalities in a wide variety of technology areas. Among them, epitaxial ferroelectric $BiFeO_3$ has demonstrated huge potential as a new visible light absorber material, pointing the way towards the manufacture of highly efficient photovoltaic devices. However, preparation of complex epitaxial oxides has been essentially limited to specific substrates, hindering the integration of such materials into practical devices on which epitaxial growth cannot be achieved. Here we develop a new solution-based process to prepare $Sr_3Al_2O_6$ sacrificial layers that can be selectively removed by H_2O. Its feasibility is tested to exfoliate solution processed $BiFeO_3$ and atomic layer deposited Al_2O_3. By means of X-ray diffraction, atomic force microscopy and scanning transmission electron microscopy, the films have been thoroughly characterized. Also, we performed a study on surface free energy and work of adhesion to transfer the active film to new surfaces, offering a novel platform to optimize the use of this sacrificial layer to freely manipulate complex oxides.

Acknowledgements

First of all, I would like to acknowledge my supervisor, Dr. Mariona Coll, who has mentored me throughout all the learning underlying this work, dedicating a lot of her time to make it possible. Thanks for her patience, readiness and advice. Also, for offering me the singular opportunity to play a role in a highly multidisciplinary cutting-edge research, which brings together my interests in applied physics, materials chemistry and nanoengineering, as well as the commitment to help develop a more sustainable and environmentally respectful society through science.

This project has been carried out thanks to the contributions of all members of CHEMOX team, at ICMAB-CSIC (Barcelona). Special thanks to Pol Sallés for his personal attention and dedication, for his collaboration in preparing and characterizing samples and, above all, for being an effective and reliable colleague, always ready to lend a hand. I would like to acknowledge Pamela Machado for training me in the use of laboratory equipment and for her example of commitment and dedication to science, and Pengmei Yu for her collaboration in the characterization of samples by SEM.

I acknowledge Roger Guzmán for acquiring the STEM images at the School of Physical Sciences, group of Prof. Wu Zhou (University of Chinese Academy of Sciences, Beijing). Also, *Servicios Centrales de Investigación* (Universidad de Málaga) for performing the thermal analysis characterization, Mariona de Palau for her help in the synthesis laboratory, the SPM Lab at ICMAB-CSIC (particularly Maite Simón) for acquiring the AFM images, and the NANOQUIM platform staff.

My stay at ICMAB-CSIC has been possible thanks to a JAE Intro scholarship granted by CSIC (*Consejo Superior de Investigaciones Científicas*, Spain). I therefore appreciate this fantastic opportunity that has allowed me to learn and mature as a scientist, combining my academic education with a valuable first-hand training at a research facility.

Finally, I would also like to acknowledge Dr. Teresa Puig, who leads the department of Superconducting and Large Scale Nanostructures, and Dr. Xavier Obradors, the director of ICMAB-CSIC, for making this project possible.

Revision history and approval record

Revision	Date	Purpose
1	11/05/2020	Document creation
2	26/05/2020	Document creation
3	03/07/2020	Concepts and style revision
4	16/07/2020	Final revision

Written by:		Reviewed and Approved by:	
Date	17/07/2020	**Date**	17/07/2020
Name	Ivan Caño Prades	**Name**	Mariona Coll Bau
Position	Project Author	**Position**	Project Supervisor

UNIVERSITAT POLITÈCNICA DE CATALUNYA BARCELONATECH

telecos BCN

Contents

List of Figures

List of Tables

1 Introduction

1.1 Statement of purpose

Complex oxides are of great interest for their rich chemical and physical properties, and their functionalities in a wide variety of technology areas, including data storage and computing, photonics, superconductivity, power electronics, and energy conversion and harvesting [14]. Among them, perovskite oxide $BiFeO_3$ is highly ferroelectric at room temperature and has shown great promise in photovoltaics by providing a unique polarization-related charge separation mechanism [15], which is thought that could lead the way towards the manufacture of a highly efficient PV device. Up to date, epitaxial $BiFeO_3$, i.e. with a preferred crystalline orientation, has shown enormous potential as photoabsorber [16, 17]. However, preparation of epitaxial complex oxides has been essentially limited to rigid substrates and high temperature treatments, hindering the opportunity to integrate such materials into flexible devices and silicon (by monolithic integration for instance), and narrowing the range of artificial heterostructures available. In this project, we aim to contribute to break this barrier, broadening the versatility of epitaxial oxides and opening the door to explore new and emerging phenomena.

The main goal of the project is to explore a low-cost and versatile innovative approach based on chemical methodologies to obtain free-standing oxide thin films. We examine different synthetic routes to prepare complex heterostructures constituted by a substrate, a sacrificial layer and the oxide film that we want to unbind from the system, and then we investigate a procedure that will allow to selectively remove the sacrificial layer, thereby obtaining a free-standing oxide [18]. Once exfoliated, we performed a study on surface free energy and work of adhesion to transfer the active film to new surfaces, building novel heterostructures and interfaces. With this, we expect to cement the first steps for the development of a viable and cost-effective technique to unlink epitaxial photoactive oxides from their growth substrates, allowing to freely manipulate them and to expand their versatility.

In particular, we use chemical solution deposition (CSD) to synthesize a water-soluble sacrificial layer, $Sr_2Al_3O_6$. Then, a $BiFeO_3$ thin film is incorporated by CSD in order to build a complex oxide heterostructure, which is thoroughly studied with structure (XRD, STEM) and surface morphology (AFM) characterization techniques. As a proof of concept, we also examine the viability of $Sr_2Al_3O_6$ as a sacrificial layer to develop free-standing Al_2O_3 films prepared by atomic layer deposition (ALD). Finally, we have performed a theoretical study to identify the design rules to achieve a successful transfer of the oxide to the desired device substrate. To the extent possible, abundant elements and non-toxic solvents have been used.

To sum up, the main objectives of the project are:

- Develop a new synthetic process to manufacture epitaxial $Sr_3Al_2O_6$ sacrificial layers

by chemical solution deposition (CSD).

- Study the compatibility of chemical methods to prepare CSD-$BiFeO_3$/$S_3A_2O_6$//$SrTiO_3$ and ALD-Al_2O_3/$S_3A_2O_6$//$SrTiO_3$ multilayer heterostructures.
- Develop a process to selectively remove the sacrificial layer and subsequently exfoliate the oxide thin film.
- Perform a theoretical study on surface energy and interfacial adhesion to identify the design rules to achieve a successful transfer of the oxide to the device substrate.

1.2 Previous work and organization

This project is framed within the general objectives and research interests of CHEMOX team at ICMAB-CSIC, under the direction of Dr. Mariona Coll, which include:

- Functional oxides for energy applications. Oxides for photovoltaics.
- Engineering thin films and nanostructures. Development of new synthetic processes and surface engineering.
- Study and implementation of chemical deposition processes: Chemical solution deposition (CSD) and atomic layer deposition (ALD).

In order to develop the new approach to prepare cost effective $Sr_3Al_2O_6$ layers and test its viability as a sacrificial layer, this project builds on the experience of the group. The preparation of CSD-$BiFeO_3$ and ALD-Al_2O_3 films are well established processes in the group [16, 19], thus they have been adapted without carrying out any further optimization.

Most of this project, including the bulk of its experimental part, has been carried out in the research facilities of ICMAB-CSIC (Barcelona). Exceptionally, STEM images and thermal analysis (TGA/DTG and DSC) have been performed by collaborators at the University of Chinese Academy of Sciences (Beijing) and Universidad de Málaga, respectively.

1.2.1 Gantt diagram

My involvement in the project covers from July 2019 to June 2020. In July 2019 I worked at ICMAB-CSIC with an academic internship from UAB (Autonomous University of Barcelona). From October 2019 to February 2020 I stayed at ICMAB-CSIC awarded with a JAE Intro scholarship from CSIC. From March until June 2020 I completed the project as a Master's degree student of UPC (Polytechnic University of Catalonia). Due to the COVID-19 pandemic, experimental activity related to this work was suspended from March to May 2020. As a contingency plan, a theoretical study to investigate the influence of interfacial energy and work of adhesion in the process to transfer the epitaxial $BiFeO_3$ film has been carried out during these months.

Tasks have been divided into four major blocks, as shown in the Gantt diagram, see Figure 1.1. Black bars designate the time invested in the major blocks. Otherwise, blue bars correspond to the sub-tasks with which the primary assignments have been organized. We aim at the following milestones (yellow diamonds):

1. Obtain a stable $Sr_3Al_3O_6$ precursor solution
2. Obtain a highly crystalline and homogeneous $Sr_3Al_3O_6$ sacrificial layer prepared by CSD
3. Manufacture a CSD-$BiFeO_3$/$Sr_3Al_2O_6$//$SrTiO_3$ heterostructure
4. Manufacture an ALD-Al_2O_3/$Sr_3Al_2O_6$//$SrTiO_3$ heterostructure
5. Exfoliate the Al_2O_3 layer by chemically removing the sacrificial layer
6. First studies to establish a general theory-based criterion, based on interfacial properties, to determine the most suitable materials to transfer and manipulate free-standing oxide layers
7. Write the complete thesis of the project

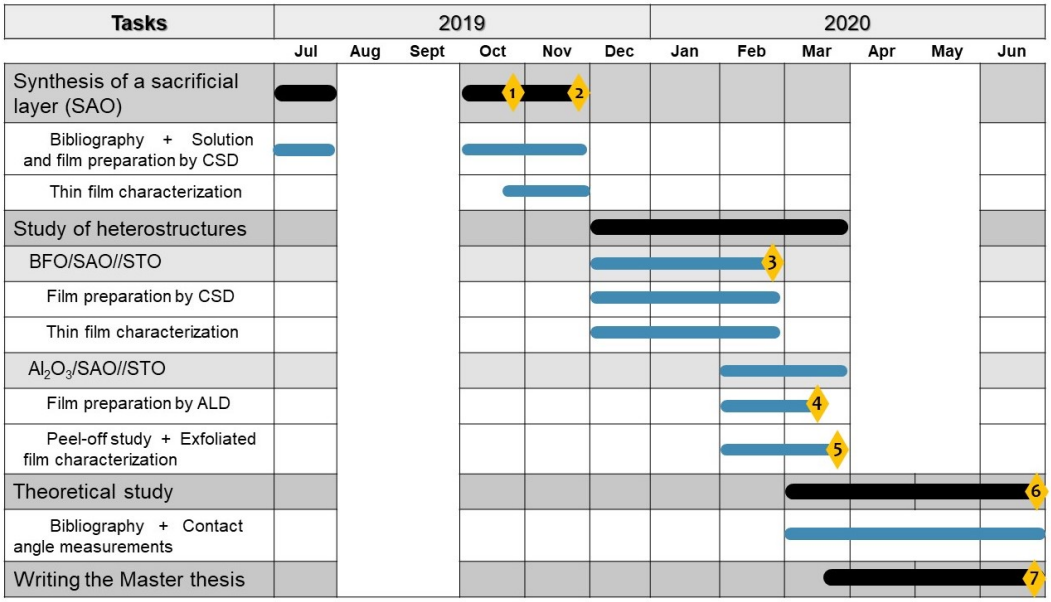

Figure 1.1: Gantt diagram of the project.

2 State of the art

2.1 Photovoltaics and ferroelectric perovskite oxides

The sun delivers more energy to Earth in one hour than humanity consumes over the course of a year [20]. In a world increasingly concerned with finding alternatives to the highly polluting and dangerous fossil and nuclear fuels, one of the most efficient ways to harvest solar energy is to convert it into electricity, and thus take advantage of its vast abundance and worldwide accessibility. Moreover, this could open the door to developing new strategies to meet the global energy demands in a clean and environmentally respectful way.

In fact, solar energy will play a key role in meeting the requirements of the Paris Agreement reached in 2015 to give an international and coordinated response to the challenges of the global climate crisis. In the context of this agreement, the *Plan Nacional Integrado de Energía y Clima 2021-2030* (PNIEC) [1] for Spain stipulates that by 2030, CO_2 emissions must have been reduced by up to a 23% with respect to 1990, and the 42% of the total energy consumption must come from renewable sources. According to this document pending approval (July 2020), it is expected that between 2020 and 2030, the installed power of solar photovoltaic technology will be doubled, see Figure 2.1.

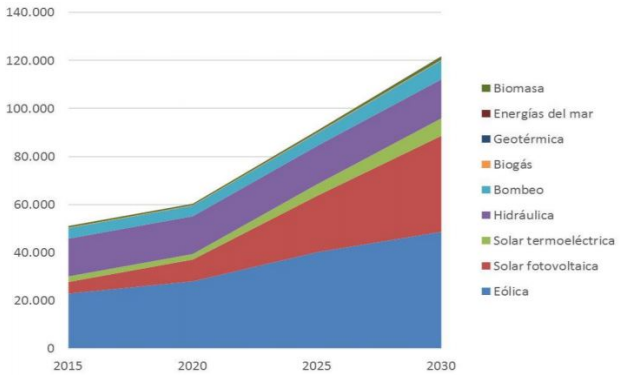

Figure 2.1: Estimated installed power of renewable energy technologies (in MW). Red corresponds to solar photovoltaics [1].

Commercial crystalline Si solar cells are widely implemented throughout the world with excellent performance. It is reported that these devices represent about a 90% of the global photovoltaic market, with power conversion efficiencies higher than 25% [21, 22]. Their photovoltaic mechanism is based on the p-n junction effect, in which the absorbed photons can pump electrons from the valence band of the light absorbing semiconductor material to its conduction band [23, 24]. Consequently, the maximum voltage these instruments can produce is limited by the electronic band-gap of the semiconductor. Also, the maximum efficiency of single-junction solar cells is theoretically limited at a $\sim$ 33% under sunlight (Sockley-Queisser limit) [25, 26]. Therefore, in order to move towards the enforcement of solar energy as a viable and efficient alternative to non-renewable power sources, it is

interesting to explore other photovoltaic materials and technologies, looking for ways to overcome the shortcomings of current devices. Notably, the family of transition metal oxides has aroused great interest for their vastity, the complexity of their correlated behaviour, and the wealth of functional properties they display, among which may be a high chemical and thermal stability, robustness and the non-toxicity of their components [27].

Ferroelectric perovskite oxides (FEPO) have emerged as some of the most promising light collector materials for solar energy harvesting [28, 29]. Having a non-centrosymmetric structure, ferroelectric perovskites provide a unique route to spontaneously separate photogenerated electron-hole pairs, known as bulk photovoltaic effect, which allows to achieve large above band-gap open-circuit voltages [30, 31, 32, 33]. Since the photovoltage is no longer limited by the transition band-gap of the semiconductor, this phenomenon is thought that could lead to efficiency values beyond predicted theoretical limits in conventional cells [34, 35]. Also, they share the same structure as organic-inorganic hybrid perovskites, which have achieved high efficiencies of up to 25.2% [21, 36] but are less stable. Nevertheless, most of these ferroelectric oxide perovskites typically absorb in the ultraviolet energy range (3-4 eV) [37, 38], far from the ideal $\sim$ 1.4 eV [39].

$BiFeO_3$ (BFO) is among the most attractive lead-free perovskite oxides to be implemented as the photoactive layer in FEPO photovoltaic devices. It is a multiferroic material, strongly ferroelectric at room temperature and presents a relatively narrow band gap of 2.7 eV [40, 41]. Interestingly, recent studies have reported that the incorporation of Co in $BiFeO_3$ yields encouraging results in further reducing the band-gap from 2.7 to 2.3 eV while showing high ferroelectric performance [16]. It has also been proven that rare earth (RE) substitution of the Bi-site minimizes the presence of secondary phases and film defects, besides contributing to a general improvement of photovoltaic and ferroelectric properties [42, 43].

However, synthesis of BFO-based devices is not without challenges. The good traits of BFO are linked to attaining an epitaxial growth of the film (preferred crystalline order) [44, 45, 46], where the crystalline structure is determined by an underlying single-crystal substrate, see Figure 2.2, and a high temperature thermal treatment [47]. Regardless the good results, using single-crystal substrates hinders the applicability and especially the manipulation of epitaxial oxide films, e.g. FEPO materials, excluding the possibility of manufacturing flexible devices or integrating them in silicon type substrates, and thus decreasing their commercial appeal. Furthermore, these very specific substrates are fragile, rigid and expensive.

Developing a new technology to unlink the complex oxide phase from the growth surface, and thus obtain a free-standing epitaxial oxide film, would represent a huge step towards the goal of achieving a highly efficient and low-cost oxide-based photovoltaic device, breaking the barrier of traditional rigid substrates. This innovative methodology would allow manipulation, integration and an unlimited use of FEPO materials, for example using flexible

substrates and using polymer and textile substrates for smart devices . Furthermore, this opportunity would open a whole new world of applications not only for photovoltaics, but also for spintronics, opotoelectronics and microelectronics [48, 49, 50].

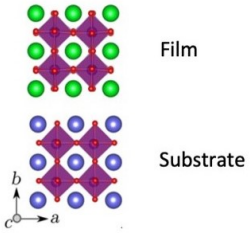

Figure 2.2: Structure of a perovskite oxide epitaxially grown on a perovskite substrate.

2.2 Free-standing epitaxial oxides

Many efforts have been devoted to developing procedures to expand the versatility of epitaxial oxide films, allowing their manipulation and integration into practical devices. These include mechanical exfoliation, dry and wet-chemical etching treatments [48, 51]. Within the latter technique, there are several variants. One of them is to destroy the growth substrate with an etchant solution that does not damage the complex oxide layer, thereby allowing to obtain a free-standing oxide film. However, this approach does not enable the substrate to be recycled. Alternatively, it is interesting to incorporate a sacrificial layer between the substrate and the complex oxide, whose removal by a chemical treatment allows both to retrieve the original single-crystal substrate and the epitaxial free-standing thin film [52, 2].

For this process to be successful, the sacrificial layer needs to meet some requirements. First, it should stand the complex oxide thermal crystallization treatment. Second, it must be selectively removed by a chemical procedure that does not damage the active oxide film. Moreover, in the case of preparing a free-standing epitaxial oxide, as in this project, the sacrificial layer should be able to transfer the epitaxy to the complex oxide. So far, promising results have been reported with (La,Sr)MnO_3, which is selectively etched by an acid blend, allowing to prepare and transfer single Pb(Zr,Ti)O_3 layers [53] and other complex architectures, such as $SrRuO_3$/Pb(Zr,Ti)O_3/$SrRuO_3$ [54]. Also, $Sr_3Al_2O_6$ (SAO) is an effective water-soluble sacrificial layer, which has been already used to transfer a wide variety of perovskite thin films and oxide structures, such as $SrTiO_3$, $SrTiO_3$/(La,Sr)MnO_3 and $BiFeO_3$ [52, 55, 2]. However, the synthesis techniques currently applied to develop and implement these oxide systems, such as Pulsed Laser Deposition (PLD) and Molecular-Beam Epitaxy (MBE), require the use of high vacuum (between 10^{-7} and 10^{-3} mbar) and high processing temperatures (600-900ºC), limiting their scalability and feasibility to be applied into mass-production assembly lines. Thus, it is crucial to find sustainable, scalable and low-cost new processes to prepare and manipulate free-standing oxides with atomic precision, more effectively and adaptively than with the current methods.

The preparation of free-standing oxides by wet-etching of a sacrificial layer is based on the following steps. See Figure 2.3 for an example using $Sr_3Al_2O_3$ as the sacrificial layer, and PDMS as a mechanical support to help release the free-standing oxide [2].

1. Development of a viable sacrificial layer
2. Build a complex multilayer heterostructure: oxide film / sacrificial layer // substrate, see Figure 2.3(a)
3. Selectively remove the sacrificial layer in order to release the top oxide film with the help of a polymer support, see Figure 2.3(b)
4. Transfer the free-standing oxide film to the desired new substrate, see Figure 2.3(c)

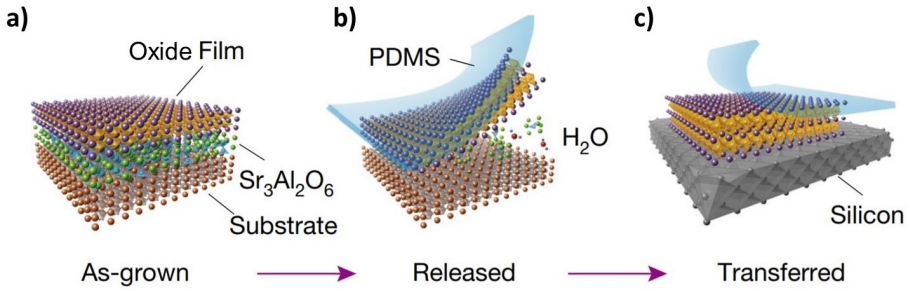

Figure 2.3: **a)** Schematic of a multilayer system with a $Sr_3Al_2O_6$ buffer layer. **b)** The sacrificial $Sr_3Al_2O_6$ layer is dissolved in water to release the top oxide film with the mechanical support of PDMS. **c)** The free-standing film is transferred to a substrate. Adapted from [2].

Once the sacrificial layer has been removed, it is important to capture the free-standing film with the mechanical support of an adherent surface, such as a polymer support, see Figure 2.3(b). However, the ultimate long-term goal is to transfer the active film to substrates with which we can build practical devices, e.g. perovskite/Si or perovskite/fabric. Therefore, an extra complexity lies in relocating the perovskite thin film from the polymer to the new substrate (silicon or otherwise). It has been reported that interfacial properties have an important role in the nanoscale mechanical properties of the thin film/substrate system, including adhesion and ease to exfoliate and transfer to a different surface [56, 57]. Hence, by selecting appropriately the polymer support and substrate, thereby taking into account the nature of the interfaces that are formed, it is expected that the handling capacity of the complex oxide could be improved.

2.3 Low-cost methodologies to prepare thin films

In the context of this research, Chemical Solution Deposition (CSD) and Atomic Layer Deposition (ALD) stand for highly appealing opportunities. They are versatile and cost-effective deposition techniques, which allow to obtain thin films with precise nano-scale control of composition and thickness.

Chemical Solution Deposition (CSD) is an overarching term used to describe any solution-based processing method, whereby a precursor solution is used to manufacture a thin film [58, 59, 60]. It is a versatile method, which provides excellent stoichiometry control and coverage of large surface areas, does not require vacuum conditions and it is relatively easy to scale up to meet the demands of industrial production processes. The procedure starts with the preparation of an homogeneous precursor solution from metalorganic compounds, which are mixed in accordance to the stoichiomety of the desired phase. Thereupon, the solution is deposited by spin-coating, followed by the removal of organic remains by drying, thermal consolidation and crystallization [61]. Finally, if epitaxy is required, the sample is subjected to a high temperature thermal treatment (rapid thermal annealing, tubular furnace or hot plate), by which the desired crystalline phase is achieved. To avoid the appearance of secondary phases, it is essential to have a deep understanding of the thermodynamic and kinetic processes that take place in the conversion [61, 62], and adjust the treatment accordingly. See Figure 2.4 for the basic steps of the procedure.

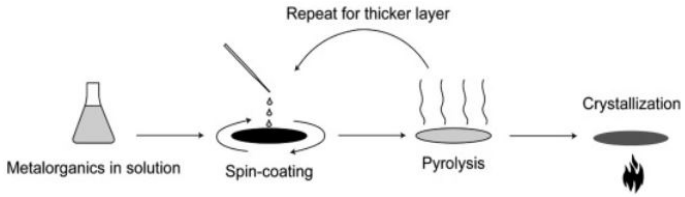

Figure 2.4: Basic process steps of the CSD method [3].

So far, CSD has proven effective in preparing thin films of some complex functional oxides with ferroelectric properties [63], such as $BiFeO_3$ [16] and $PbZr_xTi_{1-x}O_3$ [64]. It has also been successfully applied in the synthesis of superconducting and magnetic materials, e.g. $YBa_2Cu_3O_7$ and (La,Sr)MnO_3, respectively [65, 61].

On the other hand, Atomic Layer Deposition (ALD) is a low temperature (< 300ºC) and low-vacuum (10^{-2} to 10 mbar) vapor phase technique capable of producing ultrathin coatings with atomic level control of thickness and composition, and an excellent conformality on 3D surfaces. ALD relies on the alternate pulsing of gaseous chemical precursors that react with the substrate, resulting in the sequential deposition of monolayers. During each of these gas-surface reactions, the precursors are pulsed into a chamber under low vacuum for a certain optimized amount of time to allow the chemical compound to fully interact with the substrate's surface (self-limiting surface reaction). Subsequently, the chamber is purged with an inert carrier gas to remove any unreacted precursor or reaction by-products. Since every pulsing of precursors, i.e. cycle, deposits only one molecular layer, film thickness is ultimately determined by the number of cycles [66, 67, 68].

In this project we investigate for the first time the viability of CSD and ALD to manufacture thin film oxide/$Sr_3Al_2O_6$ heterostructures on $SrTiO_3$ substrates. Also, we study a procedure to selectively remove the sacrificial layer, and thus obtain a free-standing oxide thin film.

3 Experimental procedure

The experimental part of the work involves synthesizing and characterizing $Sr_2Al_3O_6$ (SAO) and $BiFeO_3$ (BFO) thin films by CSD, and amorphous Al_2O_3 by ALD. In this section, we describe in detail the procedure to obtain each of these thin films based on their composition and deposition method. Also, we present the set of characterization techniques used for their structural and morphological study.

3.1 Chemical Solution Deposition

3.1.1 Preparation of $Sr_2Al_3O_6$ thin films

In this project, we report for the first time on a procedure to obtain $Sr_3Al_2O_6$ thin films by CSD. In order to find the optimal combination of precursors and solvents to achieve the most stable, homogeneous and crystalline phase, two synthetic routes have been studied.

Nitrates route (N). Metal nitrate salts are highly soluble in water, they have a low decomposition temperature and the high-volatility of their decomposition by-products minimizes the presence of residual contaminants in the final solution [69]. Therefore, $Sr_3Al_2O_6$ films were prepared by using $Sr(NO_3)_2$ and $Al(NO_3)_3$ as chemical precursors. First, these precursors were weighted according to the stoichiometry of $Sr_3Al_2O_6$. Next, they were mixed in deionized water in order to obtain a final concentration of 0.25 M with respect to the sum of metal cations (ΣM^{n+}). Citric acid ($C_6H_8O_7$, CA) was added with a CA/ΣM^{n+} ratio of 2:1, acting as a chelating agent and also increasing the viscosity of the solution, thus improving the quality of the films. Finally, the solution was left under continuous stirring at T = 90ºC for 3 hours.

Metalorganics route (MO). Alternatively, we have also prepared $Sr_3Al_2O_6$ thin films using strontium acetate, $Sr(CH_3CO_2)_2$, and aluminium acetylacetonate, $Al(C_5H_7O_2)_3$, metalorganic precursors. In this case, the chemical precursors were dissolved in acetic acid and no complexing agents were incorporated. To improve the stability of the solution, 5% water was added. Then, the solution was left under continuous stirring at T = 60ºC for 3 hours.

In either case, deposition was performed on $SrTiO_3$ (001)-oriented substrates. $SrTiO_3$ is a centrosymmetric non-conductive substrate with a c-axis parameter of 3.905 Å (STO) [70]. For its part, $Sr_3Al_2O_6$ has a cubic unit cell with lattice constant 15.844 Å, corresponding to four $SrTiO_3$ cells ($4 \cdot 3.905 = 15.620$ Å). Indeed, the mismatch between $SrTiO_3$ and $Sr_3Al_2O_6$ is very small, amounting to a minimal -1.41%. Hence, the atomic positions on the STO (001) plane can be directly projected onto the $Sr_3Al_2O_6$ (001) plane, leading to epitaxial growth.

Finally, the sample was subjected to a high temperature thermal treatment. An optimization process was performed in order to establish the optimal annealing treatment conditions for

both synthetic routes. Samples were subjected to a heating ramp of 5-25ºC/min, followed by a 15 min - 1 h plateau at 500-900ºC, and a cooling ramp to room temperature [71].

3.1.2 Preparation of $BiFeO_3$ thin films

In this case, precursor solutions were prepared by weighting the chemical nitrate precursors, $Bi(NO_3)_3$ and $Fe(NO_3)_3$, according to the stoichiometry of the final film. Then, they were mixed in a solvent blend of 2-methoxyethanol and acetic acid in order to obtain a final concentration of 0.25 M, with respect to Bi. The solution dissolved completely after 30 minutes of stirring at T = 55ºC.

The solution deposition was performed by spin-coating in a nitrogen dry box whose humidity was less than a 10%. 20 nm thin films were manufactured by depositing 15 μl of the 0.25 M $BiFeO_3$ solution on the $Sr_3Al_2O_6$//$SrTiO_3$ structure, followed by spin-coating at 6000 rpm for 1 min. After that, they were heated at 100ºC for 10 minutes and at 300ºC for 4 minutes.

Finally, samples were subjected to a high temperature thermal treatment by flash-heating at the processing temperature, with an O_2 flow of 0.6 l/min to help in the formation of the phase. Note in Figure 3.1 that the sample is directly subjected to the $BiFeO_3$ growth temperature, 600ºC, as previously optimized by the group [16, 72].

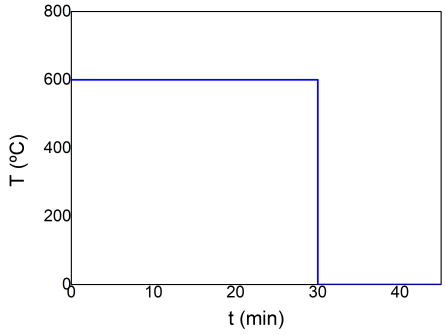

Figure 3.1: High temperature thermal treatment profile for 20 nm $BiFeO_3$ thin films.

3.2 Atomic Layer Deposition

3.2.1 Preparation of Al_2O_3 thin films

Al_2O_3 thin films preparation by ALD was performed in collaboration with other members of the CHEMOX group, at the Nanoquim Platform, ICMAB-CSIC (Barcelona).

The procedure consisted in the following steps. First of all, the substrate's surface was activated by subjecting the $Sr_3Al_2O_6$ thin film to a pre-treatment of O_3. Once the substrate was activated, deposition of Al_2O_3 layers was achieved through alternating pulses of gaseous chemical precursors. To get started, vapor trimethylaluminium (TMA) was introduced into

the reactor, adsorbing on and interacting with the substrate's surface, see Figures 3.2(a) and (b). Secondly, O_3 was added into the reaction chamber to oxidize the new surface, leading to the formation of the desired Al_2O_3 monolayer, see Figures 3.2(c) and (d).

With a growth rate per cycle of 0.12 nm/cycle, 400 cycles were carried out in order to obtain a final thickness of 50 nm.

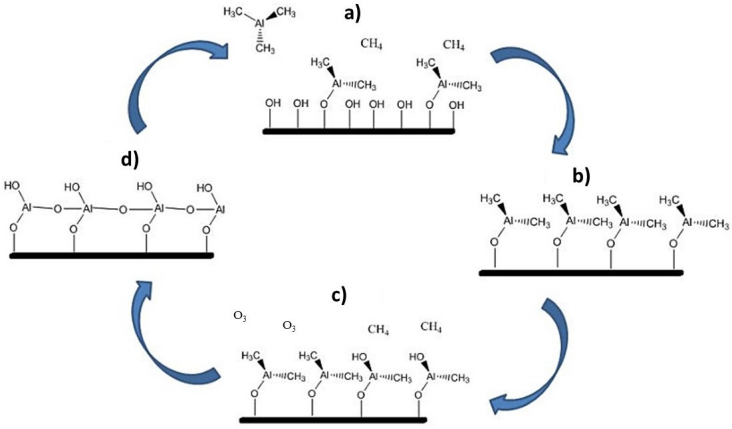

Figure 3.2: ALD growth cycle in four stages: **a)** Exposure of the first precursor (TMA) **b)** Purge of the reaction chamber **c)** Exposure of the second precursor (oxidant) **d)** a further purge of the reaction chamber. Adapted from [4].

3.3 Characterization techniques

3.3.1 Characterization of the structure

X-Ray Diffraction (XRD). XRD is a powerful nondestructive technique widely used to characterize crystalline materials. It provides information of the structure, including phase purity, texture and crystallinity. The X-ray diffraction spectrum is produced by constructive interference of a monochromatic X-ray beam scattered at certain angles from each set of lattice planes in the sample [73]. Measuring the angle corresponding to each peak θ, and knowing the wavelength of the incident beam λ, it is possible to determine the interplanar spacing of the crystal d by applying the Bragg law, see Equation 1.

$$\lambda = 2\ d\ sin\theta \tag{1}$$

In this project, routine studies of phase purity and film crystallinity have been performed by $\theta - 2\theta$ scans, first orienting the substrate STO(001) and then scanning in 2θ from 20º to 80º. The incident angle θ is fixed, while the position of the detector changes, recording 2θ values (difference between incident and reflected beams), see Figure 3.3. Our results have been obtained with the following instrument located in the X-Ray Diffraction Laboratory at ICMAB-CSIC (Barcelona): Siemens XRD Diffractometer D-5000 with Cu-K_α λ = 1.5418 Å.

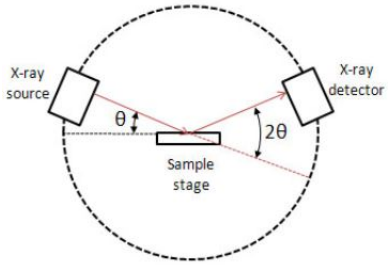

Figure 3.3: Schematic arrangement of an XRD diffractometer [5].

Scanning Transmission Electron Microscopy (STEM). STEM is a powerful microscopy technique that provides detailed information on elemental composition and crystalline structure at the atomic scale [74]. As the name implies, in STEM images are formed by transmission of an electron beam through the sample, which must be ultra-thin and transparent to electrons, usually less than 100 nm in thickness. Its operating principle consists of the following steps: An electron gun generates a beam of particles that is focused by a lens system to form an image of the electron source at the specimen (probe). Then, the probe is scanned all over the sample in a raster pattern. Finally, transmitted and scattered electrons (produced as a result of incident beam interaction with the sample) are detected, and their intensity is plotted as a function of the probe's position to configure a high resolution image [75].

STEM is compatible with different types of detectors. In particular, in this work images have been acquired by using the high-angle annular dark-field imaging mode (HAADF). The key idea behind HAADF is that of angular selection of the scattered signal, i.e. the detector's annular geometry collects only electrons scattered to large angles, note in Figure 3.4 that the HAADF detector only collects scattered electrons with angles higher that β_1. This avoids collecting the Bragg reflections and allows for images that are not subject to contrast reversals [76]. Besides, it has long been known that the Z-number dependence of the signal varies with the scattering angle [77]. Hence, HAADF imaging makes use of this property to obtain atomic-resolution images that are sensitive to the atomic number (Z).

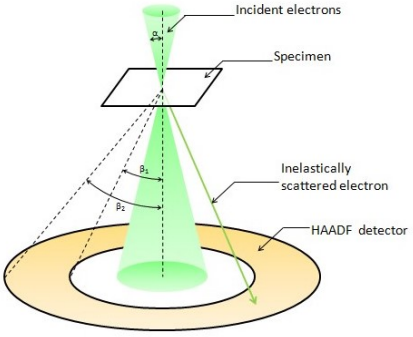

Figure 3.4: Operation principle of an HAADF-STEM detector. Inner and outer semi-angles of the annular detector are β_1 and β_2, detecting scattered electrons at high angles [6].

In this project, STEM images have been obtained from thin film cross-sections by Roger Guzmán at the School of Physical Sciences, group of Prof. Wu Zhou (University of Chinese Academy of Sciences, Beijing). In order to perform a cross-section cut of the specimen, and to reduce its thickness, samples have been processed with Focused Ion Beam (FIB). Then, aberration-corrected STEM images have been acquired with the following instrument: Nion HERMES-100, operated at 100 kV. HAADF images have been acquired using an annular detector with collection semi-angle of 92 - 210 mrad (β_1 - β_2).

3.3.2 Surface morphology characterization

Atomic Force Microscopy (AFM). AFM is a scanning probe microscopy technique, which is used in this work to characterize the surface morphology and roughness of thin films. The instrument consists of an atomically sharp tip, which is attached to a cantilever. Weak interaction forces between the sample and the probe tip cause the cantilever to deflect as the film's surface topography changes. A laser beam is then reflected from the back of the cantilever to measure its deflection. Finally, this information is fed back to a computer, which generates a topographic image [78, 79], see the working principle in Figure 3.5.

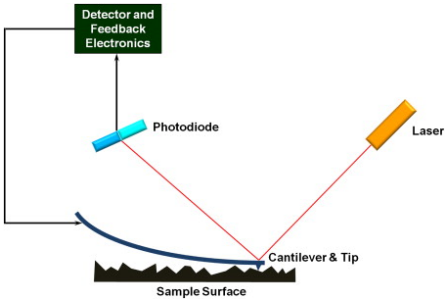

Figure 3.5: Scheme and operation principle of an AFM microscope [7].

AFM is essentially operated in two basic modes. In contact mode, the tip is dragged across the surface, holding continuous contact with the film. Otherwise, in dynamic mode the probe is vibrated above the sample. The cantilever's oscillation amplitude changes with surface topography, thus topography images are obtained by monitoring these changes.

AFM topography measurements have been performed with the following instrument located in the Scanning Probe Microscopy Laboratory at ICMAB-CSIC (Barcelona): Keysight 5100 AFM microscope. 2.5μm x 2.5μm images have been acquired and subsequently analyzed with the *MountainsMap Premium* software.

Scanning Electron Microscopy (SEM). SEM is a microscopy technique which produces images of conductive samples by scanning their surface with a focused beam of electrons. The electrons interact with atoms in the specimen, producing different signals that contain information on surface topography and composition. These interactions are divided into inelastic scattered electrons and elastic scattered electrons, resulting in secondary and

backscattered electrons respectively. The latter come from deeper regions of the sample, whereas secondary electrons originate mostly in the surface, see SEM interaction volume of the electron beam in Figure 3.6. Therefore, the two carry different types of information. Backscattered images show high sensitivity to differences in atomic number, hence allow qualitative elemental analysis. On the other hand, secondary electrons imaging can provide more detailed surface information [80, 81]. In addition to those, the electron incident beam can also produce X-rays and Auger electrons, see Figure 3.6.

Complementing the information provided by SEM imaging, Energy-Dispersive X-ray spectrometry (EDX), offers a standard procedure to identify and quantify elemental compositions in very small specimens. As mentioned above, in a SEM instrument, the atoms on the sample's surface are excited by the electron beam, emitting specific wavelengths of X-rays that are characteristic to the atomic structure of elements. An energy dispersive detector can analyze these X-ray emissions, thus performing elemental characterization [82].

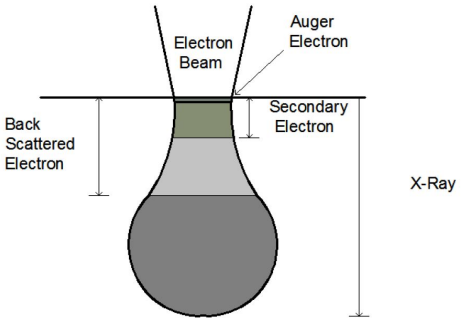

Figure 3.6: SEM interaction volume of electron beam inside the specimen [8].

SEM topography images have been obtained with the QUANTA DEI 200 FEG-ESEM instrument by the Electron Microscopy Service at ICAMB-CSIC (Barcelona). This microscope is equipped with an Energy Dispersive X-ray (EDX) system for chemical elemental analysis.

3.3.3 Thermal analysis

Thermogravimetric analysis (TGA). Thermogravimetry is a technique in which the mass of a substance (and its reaction by-products) is measured as a function of temperature and mass loss, whilst the sample is subjected to a controlled temperature program [83, 84]. This measurement provides physical information related to the thermal stability of a material, such as temperature-driven phase transitions and thermal decomposition. Additionally, from the first derivative of a TGA curve it is possible to obtain the derivative thermogravimetry (DTG) spectrum, which is of assistance when there are overlapping reactions.

Differential scanning calorimetry (DSC). DSC is a technique in which the difference in energy required to increase the temperature of a sample and a reference material is measured as a function of temperature, with both the substance of interest and reference ma-

terial subjected to a controlled thermal program [83, 84]. This technique can be used to determine the temperature at which the sample undergoes physical or chemical transformations, such as phase transitions. In particular, DSC spectra allows to identify exothermic (e.g. crystallization, crosslinking reactions) and endothermic processes (e.g. melting, glass transition), which by agreement correspond to peaks up and down, respectively.

In this project, TGA/DTG and DSC curves have been simultaneously acquired to determine at which temperature the $Sr_3Al_2O_6$ chemical precursors decompose. Measurements were performed in collaboration with *Servicios Centrales de Investigación* (Universidad de Málaga), with the following instrument: TG-DSC of Mettler Toledo + THERMOSTAR GSD320 of PFEIFFER VACUUM, equipped with an oven HT1600 and microbalance MX5. Measuring conditions consisted in a temperature program ranging from 30ºC to 1000ºC at a heating rate of 10ºC/min, with a 50 ml/min O_2 flow.

3.3.4 Contact angle measurements

In this project, contact angle measurements have been performed to obtain the surface free energy of oxide, polymer and Si surfaces. The contact angle of a solid-liquid interface can be determined by using a Drop Shape Analyzer (DSA), which allows to carry out simple measuring procedures with a high degree of automation possibilities [85]. It incorporates a manual drop deposition system, with which a small volume of a properly selected solvent is placed on the surface to study. Then, an image of the interfacial system is obtained, and specific fitting software is used to determine the contact angle. The instrument is equipped with an automatic dispenser, which makes possible to work with volumes of a few microliters, keeping a high reproducibility between replicas.

Contact angle measurements have been performed with a Drop Shape Analyzer DSA 100 from KRÜSS located at the cleanroom Nanoquim Platform, ICMAB-CSIC (Barcelona). Interface images have been analyzed with the *Drop Shape Analysis* software.

4 Study of the $Sr_3Al_2O_6$ sacrificial layer

4.1 $Sr_3Al_2O_6$ thermal analysis

$Sr_3Al_2O_6$//$SrTiO_3$ thin films have been prepared in accordance with the experimental procedure described in Section 3.1.1. In order to study the crystallization process of the films, it is important to first perform a thermogravimetric analysis. To do this, we have removed the solvents from each precursor solution using a rotary evaporator, and then we have performed TGA/DTG and DSC measurements with the dried chemical precursors, see Figure 4.1.

Nitrates route (N). TGA/DTG curves in Figures 4.1(a) and (b) show four-step mass losses. The first step, between 100ºC and 270ºC, corresponds to a mass loss of 53%, whilst the second appears in the range from 270ºC to 550ºC, with a 20% mass loss. Interestingly, an exothermic sharp peak arises simultaneously with the first step, see the DSC spectrum in Figure 4.1(c). These processes are compatible with several simultaneous phenomena. For instance, in the range from 150ºC to 400ºC, we expect processes such as dehydration and condensation of $Al(NO_3)_3$ to $Al_2O(NO_3)_3$ and $Al_2O_2(NO_3)_2$, and the release of N-based compounds (NO_2, NO, HNO_3) [86, 87]. Also, citric acid could undergo partial decomposition and transformation to aconitic acid, which would explain the exothermic behaviour [88, 89]. The second gradual mass loss is accompanied by several exothermic peaks. In this step, $Sr(NO_3)_2$, which is stable up to 280ºC, gradually decomposes to become crystalline SrO, with NO_2 and O_2 volatilization at 600ºC [90]. Finally, decomposition and $Sr_3Al_2O_6$ formation occurs from 740ºC to 900ºC, which is consistent with the large endothermic process in the DSC curve, see Figure 4.1(c).

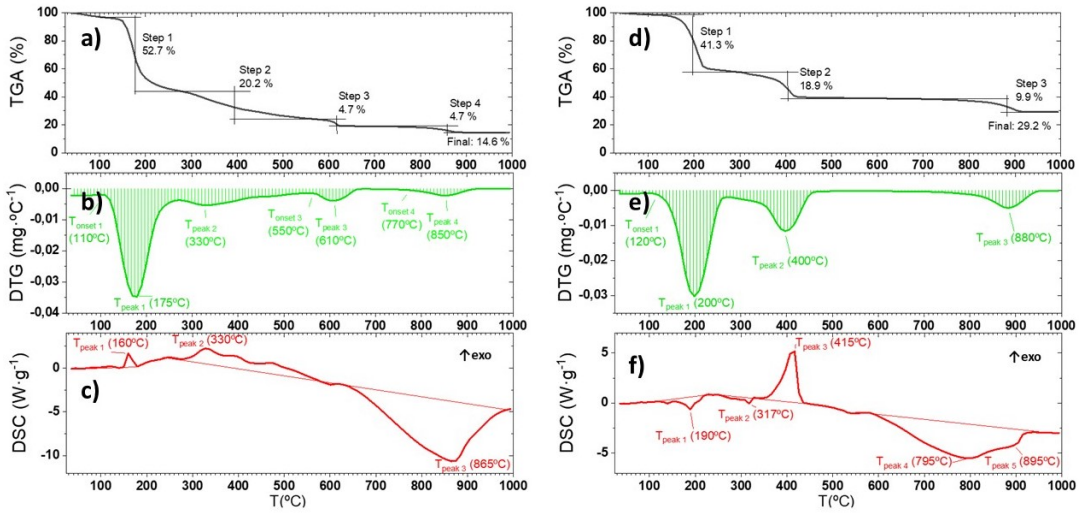

Figure 4.1: Nitrates route: **a)** TGA spectrum **b)** DTG spectrum **c)** DSC spectrum. Metalorganics route: **d)** TGA spectrum **e)** DTG spectrum **f)** DSC spectrum.

Metalorganics route (MO). In this case, three mass loss steps are detected: from 100ºC

to 270ºC (41%), from 270ºC to 480ºC (19%) and from 710ºC to 960ºC (10%), see Figures 4.1(d) and (e). The first step corresponds to an endothermic process attributed to dehydration and decomposition of aluminium acetylacetonate to Al_2O_3 [91]. The second step is most likely due to melting and decomposition of $Sr(CH_3CO_2)_2$ into $SrCO_3$, and release of CO_2 and acetone. In fact, this process is expected to result in a sharp exothermic peak [92], which is indeed verified with the corresponding DSC spectrum, see Figure 4.1(f). The final decomposition process occurs between 800ºC and 950ºC, corresponding to the transformation of strontium carbonate into SrO, thus allowing the formation of the $Sr_3Al_2O_6$ phase.

Note that in either case, the final decomposition occurs between 800ºC and 900ºC. Therefore, in order to achieve a successful $Sr_3Al_2O_6$ crystallization, it is required to subject the material to at least 800ºC. Otherwise, this thermal analysis provides a guiding idea of the decomposition process, which may slightly vary when applied to a thin film system.

4.2 $Sr_3Al_2O_6$ thin film structure and surface morphology characterization

Following the thermogravimetric analysis, $Sr_3Al_2O_6$ thin films have been prepared as described in Section 3.1.1. Upon film deposition and thermal treatment, the sample prepared from N route is homogeneous, with a flat and continuous central area, without discernible surface defects by optical microscope, see Figure 4.2(a). On the other hand, the sample prepared from MO route shows a radial pattern, with line-shaped markings extending in all directions from the centre, see Figure 4.2(b). This pattern is reported to be common in wet films manufactured from an acetate-based precursor solution, resulting from the presence of uncoordinated acetate ligands, which arrange themselves with their single polar carboxylate groups (COO^-) pointed towards the substrate. Thereby, they form a monolayer with a non-polar hydrophobic top surface, hindering a satisfactory wetting behavior [61]. Interestingly, the sample in Figure 4.2(c), where a 5% water was added to the acetate solution (MO route), no longer shows these radial patterns. Thus, it is shown that mixing solvents changes hydrophilicity, contributing to improve the morphology of the films.

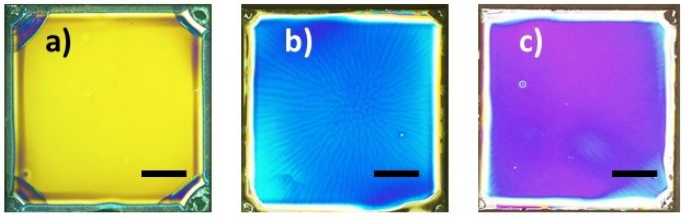

Figure 4.2: $Sr_3Al_2O_6$ thin films optical microscope images (after deposition and thermal treatment): **a)** Nitrates route **b)** Metalorganics route **c)** Metalorganics route + 5% H_2O - black scale bar = 1 mm.

From this point onward, we proceed to study in detail the samples prepared in accordance with the N and MO + 5% H_2O routes, from here on MO route.

In order to investigate the crystallinity and phase purity of the $Sr_3Al_2O_6$ samples, XRD θ-2θ scans have been performed, see Figures 4.3(a) and (b). The most intense peaks correspond to the $(00l)$ reflections of the $SrTiO_3$ substrate, whilst the smaller shoulders appearing on their left are identified as the analogous (004), (008), see Figure 4.3(b), and (0012) reflections of the $Sr_3Al_2O_6$ phase, indicating epitaxial growth. Moreover, we observe that none of the acquired spectra show any extra Bragg reflection, suggesting that we have indeed been able to induce pure-phase and epitaxial $Sr_3Al_2O_6$ growth.

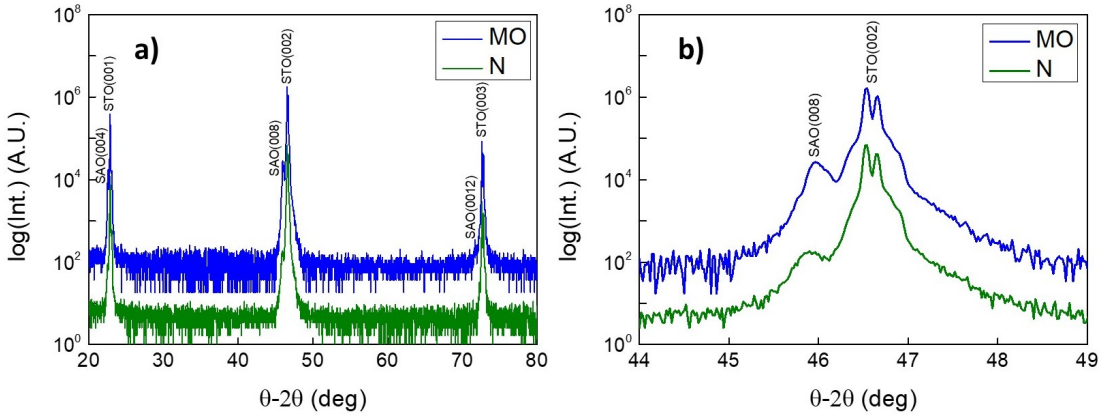

Figure 4.3: **a)** XRD θ-2θ scans of the $Sr_3Al_2O_6$ thin films prepared from: N and MO routes **b)** spectrum in the 44-49º 2θ interval.

A way to assess the accommodation between the substrate and the new phase is to determine their lattice mismatch, see Equation 2 [93], where c'_{SAO} = c_{SAO}/4, and $c_{substrate}$ = c_{STO} = 3.905 Å [70]. c'_{SAO} values have been obtained with Bragg's law (Equation 1), from the (004) and (008) 2θ angles in Figure 4.3(a). We observe that $Sr_3Al_2O_6$ experiences a minimal in-plane compressive strain, with ϵ_m less than - 1.20% in all the samples, see Table 4.1. Otherwise, we notice that there is a small difference in mismatch between the N and MO films, which could be due to a distinct quality of the crystalline phase. A reciprocal space map (RSM) should be performed to study it more thoroughly, but it is out of the scope of this project. Ultimately, from all these results we conclude that both the N and MO routes give rise to crystalline and epitaxial thin films.

$$\epsilon_m = \frac{c_{substrate} - c'_{SAO}}{c'_{SAO}} \tag{2}$$

Table 4.1: 2θ values from (004) and (008) Bragg reflections, c-axis parameter, c' and ϵ_m of the $Sr_3Al_2O_6$ thin films prepared from: N and MO routes.

Sample	2θ (004) (º)	2θ (008) (º)	c'_{SAO} (Å)	c_{SAO} (Å)	ϵ_m (%)
N	22.520	45.900	3.951 ± 0.004	15.804 ± 0.017	-1.166 ± 0.001
MO	22.579	45.963	3.945 ± 0.006	15.779 ± 0.024	-1.101 ± 0.001

Homogeneity and uniformity are other important parameters to characterize the quality of

thin films. Since the photoactive material must be deposited on the $Sr_3Al_2O_6$ layer, any underlying phase morphology defects will also spread to the top oxide film, which in turn could hamper the etching of sacrificial layer and lead to a lower photovoltaic performance of the device. Indeed, high leakage currents in oxide thin films have been attributed, among other phenomena, to the presence of grain boundaries and other morphology defects, resulting in significant variations to the optical and electrical response of the material [94, 95, 96].

To characterize the surface morphology of our thin films, AFM images have been acquired, see Figure 4.4. We notice that the sample prepared with nitrate precursors has the lowest roughness, with 2 nm (Rrms value), see Figure 4.4(a). Instead, the MO route gives rise to a higher value of 5 nm. Also, in Figure 4.4(b) we observe scattered small black spots, which could indicate that this is a porous sample. Overall, the nitrates route stands as the most promising, leading to samples with a smooth surface and low roughness.

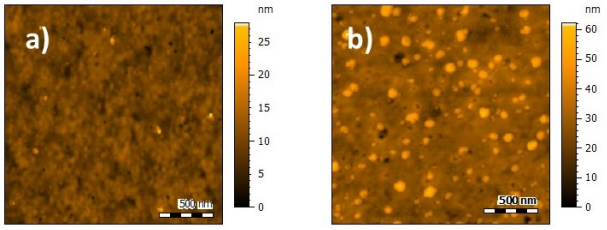

Figure 4.4: 2.5 μm x 2.5 μm AFM topography images and surface soughness (Rrms) of the $Sr_3Al_2O_6$ thin films prepared from: **a)** Nitrates route **b)** Metalorganics route.

So far we have seen that the $Sr_3Al_2O_6$ samples prepared with nitrate precursors have a homogeneous and smooth surface, with the lowest roughness and least morphology defects. Furthermore, they are highly crystalline, epitaxial and pure-phase. For these reasons, and also due to the high stability of water-nitrates precursor solutions, from now on we will focus on studying this type of thin films.

In order to further characterize the microstructure of the $Sr_3Al_2O_6$ thin film, N route, a STEM cross-section study has been performed, see Figure 4.5. We observe that the sample exhibits a highly ordered microscopic structure and textured phase, extending all the way from the $SrTiO_3$//$Sr_3Al_2O_6$ interface up to the surface, without visible amorphous areas, pores or grain boundaries. Notice in the insets of higher magnification that we have achieved an epitaxial phase, with the atoms of the material (white spots) arranged in a single-crystal lattice.

To sum up, with the present thin film characterization study we have proven that $Sr_3Al_2O_6$ films prepared by CSD are highly crystalline, epitaxial and pure-phase; no parasitic phases have been detected. Moreover, they have a homogeneous and smooth surface, and STEM cross-section shows a highly crystalline order. Therefore, we proceed to study the procedure to chemically remove this film, in order to be used as a sacrificial layer.

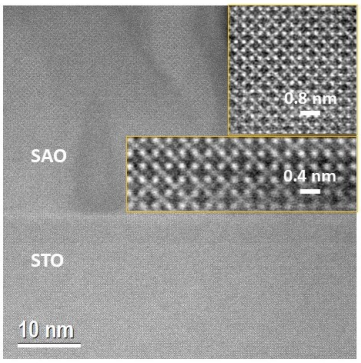

Figure 4.5: $Sr_3Al_2O_6$//$SrTiO_3$ Z-contrast cross-section STEM image - includes insets of higher magnification to show the $Sr_3Al_2O_6$ crystallographic order at the atomic level.

4.3 $Sr_3Al_2O_6$ etching by chemical solvents

One of the most important requirements of the sacrificial layer is that it can be selectively removed by a chemical treatment that does not damage the free-standing oxide, see Section 2.2. We are interested in performing tests with chemical solvents, in order to assess which one would be more appropriate to dissolve the sacrificial layer. To the extent possible, we prioritize the use of green chemicals. Accordingly, the effect of three common use solvents (acetone, methanol and water) has been examined on $Sr_3Al_2O_6$, immersing such samples in the corresponding solution for 1 min. In addition to the aforementioned common solvents, we have also studied a blend of acetic acid and 2-methoxyethanol, since it is the mixture used to prepare the precursor solution of $BiFeO_3$, this being the photoactive phase that could be interesting to obtain as a free-standing layer. The outcome of each treatment has been compared with an unscathed, as grown, sample, see Figure 4.6(a).

We observe that acetone significantly degrades the sample, although it does not completely eliminate the film, while methanol amplifies the effect of inhomogeneities at the edges, see Figures 4.6(b) and (c) respectively. On the other hand, the solvent blend of acetic acid and 2-methoxyethanol (1:3) does not seem to affect the sample, Figure 4.6(d). Finally, we verify that $Sr_3Al_2O_6$ is highly soluble in water, being that the thin film was entirely removed when we plunged the sample into Milli-Q water for 1 min, see Figure 4.6(e).

Figure 4.6: Optical microscope images of $Sr_3Al_2O_6$ thin films. **a)** as grown. Upon exposure to: **b)** acetone **c)** methanol **d)** acetic acid + 2-methoxyethanol **e)** Milli-Q water - black scale bar = 1 mm.

Therefore, we have proved that H_2O is an effective solvent to selectively remove $Sr_3Al_2O_6$ films. Since water is green and abundant, this places $Sr_3Al_2O_6$ as a highly attractive oxide to serve as a sacrificial layer. In the next section, its viability will be tested with two oxide systems: $BiFeO_3$ and Al_2O_3.

5 Study of an all-chemical heterostructure based on $Sr_3Al_2O_6$ sacrificial layer

5.1 $BiFeO_3/Sr_3Al_2O_6//SrTiO_3$ heterostructure

20 nm CSD-$BiFeO_3$ thin films have been deposited on CSD-$Sr_3Al_2O_6//SrTiO_3$ in accordance with the experimental procedure described in Section 3.1. Then, characterization of the multilayer system was performed by XRD and STEM.

In order to investigate its crystallinity and phase purity, XRD θ-2θ scans have been performed, see Figure 5.1. The orange spectrum corresponds to the $BiFeO_3/Sr_3Al_2O_6//SrTiO_3$ heterostructure and the green spectrum corresponds to a $Sr_3Al_2O_6//SrTiO$ system (N route). The most intense peaks correspond to the (001), (002) and (003) reflections of the $SrTiO_3$ substrate. We observe other peaks appearing as shoulders at 22.6º, 46.0º and 71.7º, which can be attributed to the $(00l)$ reflections of both $Sr_3Al_2O_6$ and $BiFeO_3$. However, it is difficult to unambiguously identify it, because the $Sr_3Al_2O_6$ and $BiFeO_3$ $(00l)$ Bragg reflections overlap. Otherwise, note that the spectrum does not show any extra reflection, suggesting that no secondary phases have appeared.

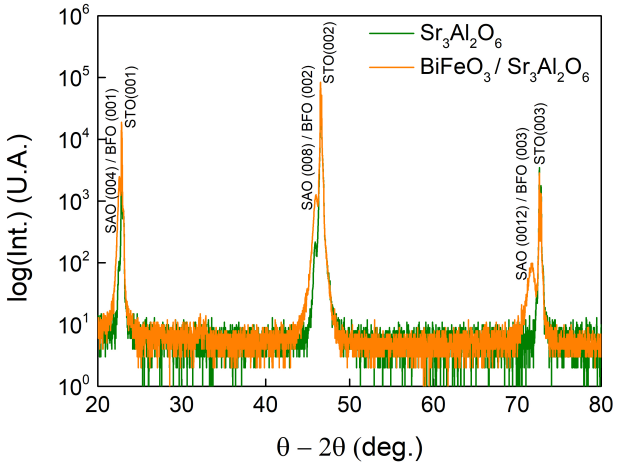

Figure 5.1: XRD θ-2θ scans of the CSD-$Sr_3Al_2O_6//SrTiO_3$ and $BiFeO_3/Sr_3Al_2O_6//SrTiO_3$ systems.

We studied the microstructure of the $BiFeO_3/Sr_3Al_2O_6//SrTiO_3$ system by acquiring STEM images from a cross-section of the sample, see Figure 5.2(a). Rather than a multilayer structure, we have obtained a nanocomposite film, in which perfectly square-shaped particles have appeared inside a matrix of 60 nm films. Therefore, it is shown that no $Sr_3Al_2O_6$ intact film remains after $BiFeO_3$ deposition by CSD.

In order to further characterize the structure, high-angle annular dark-field (HAADF) images were acquired. This high-resolution microscopy imaging mode provides elemental composition and crystalline order information at the atomic scale, see Figure 5.2(b). We notice that

the nanoparticles are also constituted by crystalline phase, note the highly ordered atomic arrangement. Furthermore, the HAADF detector is very sensitive to variations in the atomic number, allowing to obtain Z-contrast scanning images to perform elemental analysis. In Figure 5.2(b) we observe several snapshots from the same region of the sample, but different areas are colored with brighter tones depending on the concentration of the indicated element (Sr, Al, Fe or O). Accordingly, we realize that the inset square-shaped particles are especially rich in Sr and Al, whilst the matrix contains mostly Fe and O. Therefore, it is likely that by adding $BiFeO_3$, the $Sr_3Al_2O_6$ layer dissolves within the new phase.

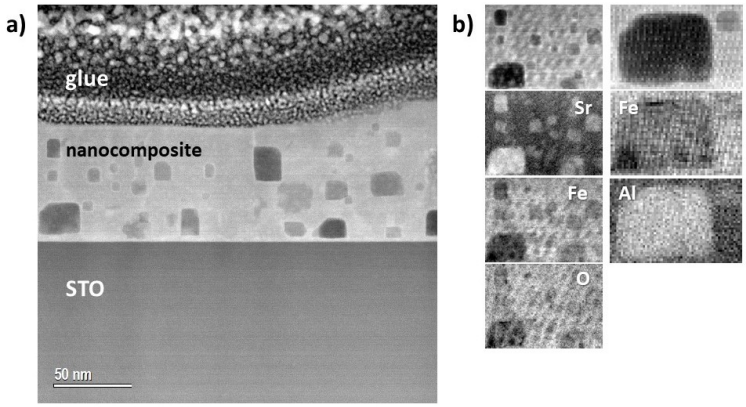

Figure 5.2: **a)** Cross-section STEM images of $BiFeO_3/Sr_3Al_2O_6//SrTiO_3$ heterostructure **b)** High-angle annular dark-field (HAADF) images.

To sum up, here we have shown that $BiFeO_3$ deposition on $Sr_3Al_2O_6$ by CSD gives rise to a nanocomposite material, where Sr and Al-rich square-shaped nanoparticles arise inside a $BiFeO_3$-rich matrix. Also, both the particles and matrix are crystalline phases. This interesting discovery encouraged us to investigate ALD as a low-temperature alternative deposition methodology to obtain free-standing oxides, preserving the integrity of $Sr_3Al_2O_6$ and minimizing interdiffusion between the two phases. As a proof of concept, in this project we have used a binary oxide, Al_2O_3, prepared by ALD.

5.2 $Al_2O_3/Sr_3Al_2O_6//SrTiO_3$ heterostructure

Al_2O_3 has been deposited by ALD on CSD-$Sr_3Al_2O_6//SrTiO_3$ in accordance with the experimental procedure described in Section 3.2. Unlike CSD, with ALD we work at a lower temperature (250ºC), which helps to avoid diffusion between phases. Also, it is a process based on the deposition of precursors in the gas phase, annulling the possibility of dissolving the $Sr_3Al_2O_6$ layer with solvents of the upper layer. Upon Al_2O_3 deposition, our next step is to assess whether we can obtain an Al_2O_3 free-standing film by developing a procedure to selectively remove the $Sr_3Al_2O_6$ buffer, while capturing the binary oxide with the mechanical support of a polymer substrate, see Figure 2.3 in Section 2.2.

5.2.1 Exfoliation procedure to obtain a free-standing Al_2O_3 layer

In order to achieve an effective exfoliation of the free-standing oxide, it is essential to take some aspects into consideration. First, in order to allow the etchant solution (water) to dissolve the sacrificial layer, we have seen that it is necessary to coat the edges of $Sr_3Al_2O_6$ with PMMA (Poly(methyl methacrylate)) before depositing the Al_2O_3 film, see Figure 5.3(a). This edge masking is crucial to prevent the borders of the sample from being completely wrapped by Al_2O_3 during the ALD deposition. PMMA coating is accomplished by spreading liquid polymer along the edges of the $Sr_3Al_2O_6$ film with a syringe, then placing the sample on a hot plate and subjecting it to a thermal treatment of 180ºC for 1 minute, whereby the resin is hardened [97, 98].

Once the Al_2O_3 film has been deposited, see Figure 5.3(b), the PMMA mask needs to be removed. Thereby, the edges of the sample are again exposed and water can easily etch the $Sr_3Al_2O_6$ layer, see Figure 5.3(c). PMMA is dissolved by immersing the sample into an acetone bath for 24 hours [99]. Note in Figure 5.3(d) that neither the Al_2O_3 (purple film) nor the $Sr_3Al_2O_6$ (yellow) are significantly damaged after the acetone cleaning treatment.

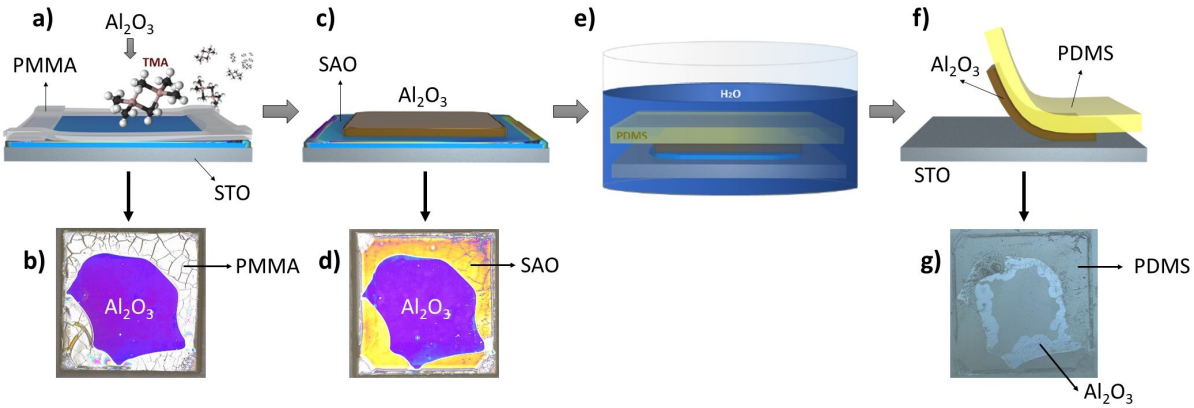

Figure 5.3: Scheme of the process to obtain free-standing Al_2O_3 films: **a)** PMMA coating and ALD-Al_2O_3 deposition **b)** Optical microscope image of an $Al_2O_3/Sr_3Al_2O_6//SrTiO_3$ system after PMMA coating **c)** PMMA removal - Al_2O_3 thin film **d)** Optical microscope image of the $Al_2O_3/Sr_3Al_2O_6//SrTiO_3$ system after PMMA removal with acetone **e)** Immersion in Milli-Q water of the PDMS supported $Al_2O_3/Sr_3Al_2O_6//SrTiO_3$ heterostructure for $Sr_3Al_2O_6$ etching **f)** PDMS/Al_2O_3 separation from $SrTiO_3$ substrate **g)** Optical microscope image of Al_2O_3 transferred to PDMS.

Finally, a piece of PDMS (Polydimethylsiloxane) (cross-linker:prepolymer [1:10]) [2, 52, 100] is attached over the sample in order to assist retrieving the free-standing Al_2O_3 film once water has etched the sacrificial layer, offering a support to which the oxide can adhere. Therefore, the system is plunged into a beaker filled with Milli-Q water for 12 hours to 2 days in order to dissolve the $Sr_3Al_2O_6$, see Figure 5.3(e), after which we separate the PDMS from the $SrTiO_3$ substrate, see Figure 5.3(f). Through this procedure, we have managed to partially exfoliate the oxide film. Note in Figure 5.3(g) that some Al_2O_3 areas

have been indeed successfully transferred to the polymeric support.

Morphology and composition characterizations of the exfoliated layer have been performed by SEM and EDX. In order to carry out observations with SEM it is necessary to use a conductive substrate. Thus, we transferred the exfoliated Al_2O_3 to a strip of conductive carbon tape, see Figure 5.4(a). On the left side of Figure 5.4(b) we see the Al_2O_3 layer transferred to the C tape (SEM). If we look at the shape of the film, we note that it corresponds exactly to that we had before on PDMS (see the right side of Figure 5.4(b)), indicating that it has been satisfactorily transferred to the conductive carbon stripe. Note in Figure 5.4(c) that the thin film appears mostly intact, which denotes that the peel-off mechanism has not caused significant damage.

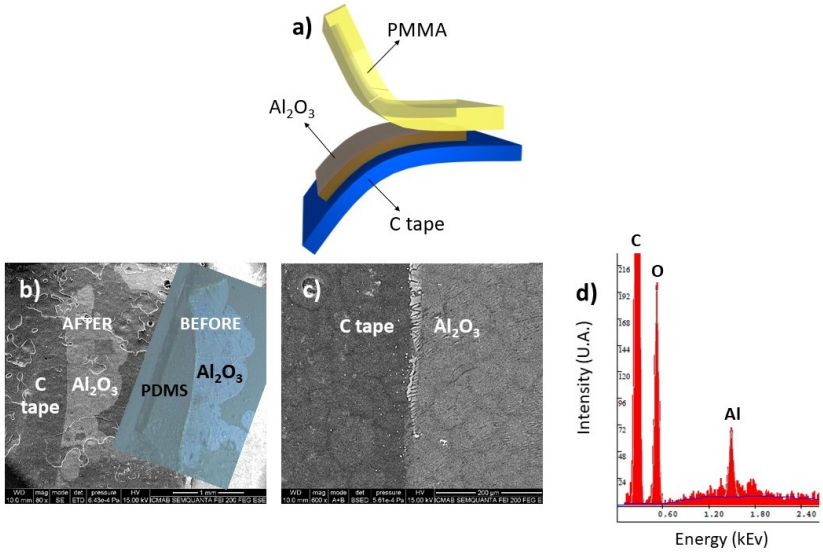

Figure 5.4: **a)** Scheme of the transfer procedure of an Al_2O_3 thin film from PDMS to a strip of conductive C tape. SEM-EDX analysis of the transfer-printed film: **b)** SEM image, 60 X - includes an image of PDMS support with Al_2O_3 layer **c)** SEM image, 600 X **d)** EDX spectrum obtained from the transferred layer on carbon tape.

The composition of the exfoliated film was analyzed by EDX. This technique allows to perform qualitative elemental analysis of the sample, see spectrum in Figure 5.4(d). We have detected the presence of C, O and Al. The carbon signal comes from the tape, however the aluminium signal clearly indicates that the sample contains this element, which would be consistent with being transferred the Al_2O_3 thin film.

In conclusion, we have proved that ALD Al_2O_3 thin films can be successfully exfoliated from a multilayer system by water etching of $Sr_3Al_2O_6$. Furthermore, these results make versatile and low-cost ALD an attractive candidate to synthesize free-standing oxides, which could help unlock the whole potential of this novel technology, allowing implementation into a wide spectrum of applications, including photovoltaics.

However, as we have seen, achieving a complete transfer of the free-standing oxide is not easy. Thus, it is interesting to study the nature of the interfaces involved in the exfoliation mechanism in order to optimize it and to offer a new platform to transfer the free-standing oxide to novel substrates, with which we can build practical devices, such as Si or intelligent textiles. In light of this, we perform a theoretical study on surface effects and adhesion phenomena, moving towards the goal of finding a general theory-based criterion, based on interfacial properties, to determine the most suitable materials to transfer and manipulate free-standing oxide layers.

6 Theoretical study on surface energy and work of adhesion to optimize the transfer of the thin film oxide

In order to develop a first approximation towards a theory-based criterion for determining the aptest supports to handle and transfer free-standing oxides, here we have examined the concepts of surface energy and interfacial adhesion applied to the heterostructures that we have studied in the project. In particular, we have investigated the following oxide/substrate systems: Al_2O_3/PDMS, Al_2O_3/Si, $BiFeO_3$/PDMS and $BiFeO_3$/Si. The interest in Si arises from the fact that excellent PV performance has been reported with perovskite/silicone tandem solar cells (halide pervoskites) [101]. Therefore, it is also very interesting to explore new mechanisms to transfer epitaxial perovskite oxides to Si, taking advantage of the good absorption properties of Si and the above open-circuit voltages of $BiFeO_3$.

With this goal in mind, the present section consists of two clearly differentiated parts. First, we carry out a strictly theoretical study on surface energy and work of adhesion, headed towards identifying the design rules to achieve a successful transfer of the oxide film to a hypothetical substrate. Secondly, we examine the specific cases of the surfaces mentioned above. In order to determine the work of adhesion of the interfaces, we have performed contact angle measurements and calculated the surface free energy of each material.

6.1 Calculation of Surface Free Energy (SFE) of a solid

The surface free energy (SFE) of a solid is a parameter of great importance in the study of interfacial systems, since it has consequential repercussions to the wettability, adhesion and reactivity of the material. In fact, “surface engineering” is now considered as an independent field of science [102], with prominent implications in materials science, nanotechnology, microelectronics, and other disciplines in which interacting with a surface plays a key role in the development of new applications.

A very simple, empiric way of evaluating surface properties of a material is by calculating the contact angle (θ) of its surface with a selected solvent. Interestingly, the relation between surface energy and contact angle has been known for more than 200 years by Thomas Young (1773-1829) [103]. See Equation 3 (Young equation), where γ_s is the SFE of a solid, γ_l is the surface tension of a liquid and γ_{sl} is the interfacial energy of the system solid-liquid.

$$\gamma_s = \gamma_{sl} + \gamma_l \, cos\theta \tag{3}$$

Quantities γ_l and θ can easily be measured, see Figure 6.1 [104] for a visual definition of the Young contact angle. However, γ_{sl} is generally unknown. Therefore, in order to determine γ_s, we need more equations.

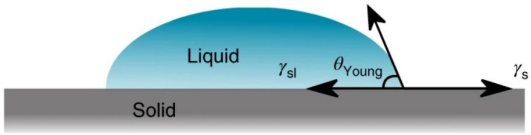

Figure 6.1: The angle formed by the intersection of the liquid-solid and liquid-vapor interfaces, geometrically acquired by applying a tangent line from the contact point along the liquid-vapor interface, is defined as the Young contact angle, θ [9].

From the quantities in Equation 3, it is possible to define an expression for the work of adhesion of a solid-liquid system. See Equation 4 (Dupré relationship), where W_{adh} is the work of adhesion.

$$W_{adh} = \gamma_s + \gamma_l - \gamma_{sl} \tag{4}$$

This expression can be generalized to any system consisting of two phases A and B, see Equation 5 [105].

$$W_{adh} = \gamma_A + \gamma_B - \gamma_{AB} \tag{5}$$

Combining Equations 3 and 4, we find the Young-Dupré equation, which relates the work of adhesion with the contact angle θ, see Equation 6.

$$W_{adh} = \gamma_l \, (1 + cos\theta) \tag{6}$$

These expressions allow us to establish relations between different parameters of interest in the study of an interfacial system. However, in order to determine the value of γ_s we need to apply some empirical approach or approximation. In the following sections, we describe three experimental methods based on the calculation of θ to determine SFE. Additionally, we review a theoretical procedure to estimate γ_s from extrapolating data of polymer melt.

The Zisman model

Developed by W.A. Zisman, this is the one of the simplest methods to calculate the SFE of a solid [106]. This model assumes that the surface energy of a solid is equivalent to its critical surface tension γ_c, which corresponds to the γ_l value of a liquid for which the contact angle with the aforementioned solid is 0º.

The γ_c value can be easily obtained from a $cos\theta$ vs. surface tension plot. First, the contact angle is measured using a series of solvents of different nature and wettability, as long as a drop can be formed at the solid-liquid interface. Then, these values are represented in the form of $cos\theta$ against the corresponding surface tension, and an extrapolation is performed to determine the value of γ_l for which $cos\theta = 1$, thus $\theta = 0$º. Right at this point, $\gamma_l = \gamma_c \approx \gamma_s$, see Figure 6.2 for an example of a basic Zisman plot.

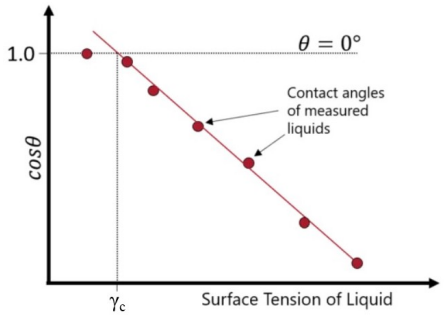

Figure 6.2: Zisman plot: $cos\theta$ vs. surface tension [10].

The Zisman model has the advantage of being very simple from a conceptual point of view. Also, its application only requires a series of contact angle measurements and a linear extrapolation. Other than that, the method proposed by Zisman does not take into account the effect of polar interactions, thus a different approach should be considered to determine the SFE of polar surfaces.

Equations of state

So far we have seen that γ_{sl} is a parameter which depends on the properties of an interfacial system consisting of a solid and liquid. This is reflected in the so-called equation of state, see Equation 7 [107].

$$\gamma_{sl} = f(\gamma_s, \gamma_l) \tag{7}$$

Finding a consistent and justified formulation for this equation of state has been the subject of numerous studies. For example, according to D. Berthelot [108], γ_{sl} can be calculated from Equation 8. Likewise, Grifalco and Good reformulated Berthelot's equation by introducing and interaction parameter Φ [109], see Equation 9.

$$\gamma_{sl} = \gamma_s + \gamma_l - 2\sqrt{\gamma_s\,\gamma_l} \tag{8}$$

$$\gamma_{sl} = \gamma_s + \gamma_l - 2\,\Phi\,\sqrt{\gamma_s\,\gamma_l} \tag{9}$$

The interaction parameter Φ is defined in accordance with Equation 10, where V_s and V_l correspond to the molar volume of each component of the system (solid and liquid). Nonetheless, in the case of an interfacial system, in which both components interact equally, it can be assumed that $\Phi \approx 1$.

$$\Phi = \frac{4\,(V_s V_l)^{\frac{1}{3}}}{\left(V_s^{\frac{1}{3}} + V_l^{\frac{1}{3}}\right)^2} \tag{10}$$

Combining any of these equations with the Young Equation 3, we find an expression where γ_s only depends on γ_l and the contact angle θ, which can be easily measured. For example, using the Berthelot Equation 8, we find Equation 11.

$$\gamma_s = \gamma_l + \frac{(1+cos\theta)^2}{4} \tag{11}$$

A.W. Neumann derived three other forms of the equation of state, see Equations 12, 13 and 14, where $\beta_1 = 1.247 \cdot 10^{-4}$ and $\beta_2 = 1.057 \cdot 10^{-4}$ [107, 110]. However, these β coefficients have been determined experimentally, which raises doubts as whether they are universal constants or empirical quantities obtained as a result of iterative procedures. Consequently, the use of these equations remains shrouded in some controversy.

$$\gamma_{sl} = \frac{\sqrt{\gamma_s} - \sqrt{\gamma_l}}{1 - 0.015\sqrt{\gamma_s \gamma_l}} \tag{12}$$

$$\gamma_{sl} = \gamma_s + \gamma_l - 2\sqrt{\gamma_s\,\gamma_l} \cdot e^{-\beta_1(\gamma_l - \gamma_s)^2} \tag{13}$$

$$\gamma_{sl} = \gamma_s + \gamma_l - 2\sqrt{\gamma_s\,\gamma_l} \cdot \left(1 - \beta_2(\gamma_l - \gamma_s)^2\right) \tag{14}$$

The Fowkes model

The most common method to compute the SFE of polar surfaces is the Fowkes model [10]. According to this model, the problem can be approached by separating the surface energy of a solid into its components: dispersive (Van der Waals interactions) and polar [111], see Equation 15, where γ_s^D and γ_s^P are the dispersive and polar components of γ_s respectively.

$$\gamma_s = \gamma_s^D + \gamma_s^P \tag{15}$$

Although it is usual to reduce the system to dispersive and polar interactions, in more general terms all interactions involved in the system should also be considered: induced (γ_s^{ind}), hydrogen bond (γ_s^H), acid-base (γ_s^{AB})... , see Equation 16 [112].

$$\gamma_s = \gamma_s^D + \gamma_s^P + \gamma_s^{ind} + \gamma_s^H + \gamma_s^{AB} + ... \tag{16}$$

Combining the Dupré Equation 4 and the Berthelot Equation of state 8, we find the following expression for the work of adhesion,

$$W_{adh} = 2\sqrt{\gamma_s \gamma_l}$$

Considering the Fowkes theory (Equation 15), we can rewrite the expression for W_{adh}, so that it depends on the dispersive and polar components of γ_s and γ_l, see Equation 17.

$$W_{adh} = 2\left[\sqrt{\gamma_s^D \gamma_l^D} + \sqrt{\gamma_s^P \gamma_l^P}\right] \tag{17}$$

Now, we use the Young-Dupré Equation 6 to get to an expression in which only γ_s, γ_l and θ appear, see Equation 18.

$$\frac{\gamma_l(1+cos\theta)}{2} = \left[\sqrt{\gamma_s^D \gamma_l^D} + \sqrt{\gamma_s^P \gamma_l^P}\right] \tag{18}$$

Thus, in order to find the SFE of a solid it is necessary to use two different liquids of which the surface tension is known, determine the contact angle between each of these two liquids and the solid, and then solve the following system of equations,

$$\frac{\gamma_{l,1}(1+cos\theta_1)}{2} = \left[\sqrt{\gamma_s^D\gamma_{l,1}^D} + \sqrt{\gamma_s^P\gamma_{l,1}^P}\right]$$

$$\frac{\gamma_{l,2}(1+cos\theta_2)}{2} = \left[\sqrt{\gamma_s^D\gamma_{l,2}^D} + \sqrt{\gamma_s^P\gamma_{l,2}^P}\right]$$

In such a way, we obtain both the dispersive and polar components of γ_s.

An easy way to tackle this problem is using a solvent whose surface tension has no polar component. For example, chloroform has a surface energy of $\gamma_l^D = 27.2$ mN/m, with $\gamma_l^P = 0$ [113]. In this case, γ_s^D can be trivially calculated with Equation 19. As a second solvent to determine γ_s^P it is usual to work with water ($\gamma_l^D = 26.4$ mN/m, $\gamma_l^P = 46.4$ mN/m).

$$\gamma_s^D = \frac{\gamma_l^D(1+cos\theta)^2}{4} \tag{19}$$

So far, we have seen three experimental methods to determine the SFE value of a solid. In each of them, the basis lies in carefully choosing one or more solvents and determining the contact angle between these liquids and the surface of the solid. Likewise, it is necessary to know the surface tension values of the selected solvents. The measurements of the contact angles can be performed with a drop shape analyzer equipment, see Section 3.3.4.

Estimation of γ_s from extrapolating data of polymer melt

Interestingly, it is possible to obtain an approximate value of SFE for solid polymers from extrapolating data of the melt, and more specifically, from the parachor constant of the liquid polymer. This allows to compute an estimate γ_s without carrying out experimental contact angle measurements, which might be useful to make a preliminary theoretical assessment of what materials are best suited for a given application. The parachor is an empirical constant that relates surface tension to the molar volume (V) of a polymer, see Equation 20. Furthermore, it is considered to be an additive quantity, thus it can be approximately expressed as the sum of empirical increments P_{Si} corresponding to single atoms or groups, and bond contributions in the molecule [114, 115].

$$P_S = \gamma^{1/4}\,V = \sum P_{Si}\ \text{(atomic contributions)} + \sum P_{Si}\ \text{(bond contributions)} \tag{20}$$

Due to the fact that the extrapolation of surface tensions of melts at room temperature leads to reliable values for a solid polymer, the SFE of solid polymers may indeed be calculated from the parachor per structural unit by applying Equation 20 [116]. Consider the following example, where we determine an estimate value of SFE for PDMS.

EXAMPLE: estimation of γ_s (PDMS) from parachor

First, we calculate the molar volume from the molecular weight of the repeat unit (74 g/mol) and density (0.97 g/ml) at room temperature. Thus, we find $V = 76.3$ ml/mol [117]. Next, we determine the parachor of the polymer from the corresponding contributions of atoms and functional groups in accordance with Sugden et al (1924), see Table 6.1. Consider the structure of the repeating unit in PDMS, see Figure 6.3 [118].

Table 6.1: Parachor contributions of atoms and functional groups in PDMS [11, 12].

	P_S
Si	25.0
2 (CH_2 + H)	112.2
O	20.0
TOTAL	157.2

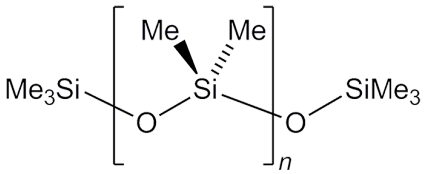

Figure 6.3: Chemical structure of PDMS monomers.

Using Equation 20, we find the following result for an estimate value of γ_s,

$$\gamma_s \text{ (PDMS)} = \left(\frac{P_S}{V}\right)^4 = 18.0\ mN/m$$

Which shows good agreement with direct measurements of polymer melt at 20ºC, ranging from 16.0 mN/m to 20.0 mN/m, depending on the polymer molecular weight [119].

Up to here, we have considered different procedures to determine the SFE, by contact angle measurements and from extrapolating data of polymer melt, the latter only pertinent for polymers. In order to assess whether free-standing oxide transfer from a polymer support to the device substrate is within possibility, we need to quantify their adherence, which can be determined by computing the work of adhesion, W_{adh}.

6.2 Work of adhesion between two solids

The reversible work of adhesion W_{adh} gives a quantitative measure of the adherence between two surfaces, see the Dupré relationship in Equation 5. In the case of an interfacial

system constituted by two solids, see Equation 21 [116], where γ_{S_1} and γ_{S_2} are the SFE of each component, and $\gamma_{S_1S_2}$ is the interfacial tension.

$$W_{adh} = \gamma_{S_1} + \gamma_{S_2} - \gamma_{S_1S_2} \tag{21}$$

γ_{S_1} and γ_{S_2} can be easily determined applying any of the experimental methods described in Section 6.1, or, in the case of polymers, from the tabulated parachor values. On the other hand, $\gamma_{S_1S_2}$ can be calculated from a generalized Grifalco and Good Equation 22, where it can be assumed that $\Phi \approx 1$.

$$\gamma_{S_1S_2} = \gamma_{S_1} + \gamma_{S_2} - 2\,\Phi\,\sqrt{\gamma_{S_1}\,\gamma_{S_2}} \tag{22}$$

Considering the Fowkes theory, W_{adh} can be approximated as in Equation 23, where $\gamma_{S_i}^D$ and $\gamma_{S_i}^P$ are the dispersive and polar components of each surface.

$$W_{adh} \approx 2\left[\sqrt{\gamma_{S_1}^D\gamma_{S_2}^D} + \sqrt{\gamma_{S_1}^P\gamma_{S_2}^P}\right] \tag{23}$$

Moreover, we can investigate how W_{adh} varies in different environments. For example, if an interface S_1-S_2 is immersed in a liquid L, its work of adhesion must be calculated in accordance with Equation 24, where γ_{S_iL} are the interfacial energies solid-liquid corresponding to each surface. This allows to modify the fundamental interactions between two surfaces, opening the door to promoting or avoiding their detachment by changing the nature of the environment in which the interface is placed.

$$W_{adh} = \gamma_{S_1L} + \gamma_{S_2L} - \gamma_{S_1S_2} \tag{24}$$

γ_{S_iL} can be determined from the SFE of each solid and the surface tension of the liquid by applying Equation 9.

W_{adh} is the work required to separate S_1 and S_2. If the work of adhesion is negative, separation between these two solids is favoured, thus will occur spontaneously. Instead, if W_{adh} > 0, the higher, the more work must be done to detach both surfaces. Hence, to transfer a thin film from a certain substrate 1 (with which W_{adh} is already positive) to another substrate 2, it is necessary that the adhesion with the second be higher. Otherwise, the thin film will remain adhered to substrate 1, with which it forms a system of larger adhesion.

Therefore, we have shown that W_{adh} allows to characterize the adhesion between two surfaces as a quality strictly dependent on interfacial properties, which in turn can be assessed by computing the SFE of the solids involved in the system (contact angle measurements). This theory provides a fundamental criterion to rationalize the manipulation procedure of free-standing oxides, according to which it is feasible to carry out transfer between substrates whose work of adhesion with the oxide film is > 0, and as long as W_{adh} with the first

substrate is lower than that with the second, see Figures 2.3 **b)** and **c)**.

In the case of a polymeric mechanical support to help transfer free-standing thin films, it is opportune that W_{adh} > 0, since we want the active film to get adhered to a new holder once the sacrificial layer has been selectively removed. Still, to further expand its manipulability, we need this new system not to be permanent. For instance, we have proved that PDMS is a good support for Al_2O_3, yet in order to broaden the possibilities of implementing free-standing oxides into diverse functional devices, we must find mechanisms to build new heterostructures, transferring the film to different substrates, such as crystalline Si. According to the set out above criterion, to achieve this transfer successfully, it is necessary that the work of adhesion of Al_2O_3 with Si be positive and higher than that with PDMS. To check the viability of this transfer, in the next section we have determined the W_{adh} of the Al_2O_3-PDMS and Al_2O_3-Si systems, by means of contact angle measurements and under different conditions and environments. In addition, we have also determined the W_{adh} of $BiFeO_3$-PDMS and $BiFeO_3$-Si interfaces, as the ultimate goal would be to be able to grow and transfer $BiFeO_3$ films.

6.3 Study of PDMS/oxide/Si interfaces for free-standing layer transfer

In the present work, we have proved that an Al_2O_3 thin film can be successfully peeled-off from its growth substrate and subsequently transferred to PDMS by water etching of CSD-$Sr_3Al_2O_6$ sacrificial layers. To go one step further, here we are interested in theoretically assessing whether it is viable to transfer a free-standing oxide film (Al_2O_3 or $BiFeO_3$) from PDMS to Si, and under what conditions. To carry out this study, we analyze in detail the nature of interfaces 1 and 2 from Figure 6.4, with a distinc interest in their work of adhesion.

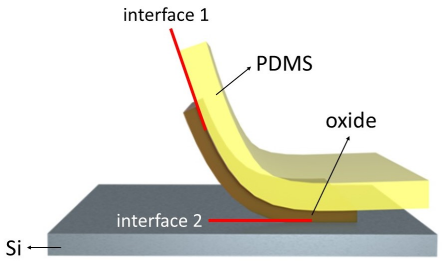

Figure 6.4: Scheme of PDMS/oxide/Si interfaces.

Therefore, we will compute the work of adhesion of each surface in order to verify whether it is higher for the oxide/Si system (which, as shown before, indicates that the transfer is favorable). Moreover, we will consider two kinds of surface for each material: bare surface and UV-ozone treated. UV-ozone cleaning is a highly effective procedure to remove contamination on the surface of a sample, especially organic residues. By applying a high-power UV light source, O_3 is generated, which then breaks down surface contaminants into volatile compounds. Remarkably, during the cleaning process, O_3 and oxygen radicals might re-

act with water molecules present in the air, resulting in the formation of hydroxide radicals, which in turn can interact with the surface. This leads to the formation of hydroxide groups, thus increasing the polarity of the sample [120]. Hence, SFE and W_{adh} are expected to vary in applying a UV-ozone treatment.

First, we have measured the contact angles of Al_2O_3, $BiFeO_3$, PDMS and Si surfaces (bare and UV-ozone treated) with Milli-Q water and chloroform. These have been obtained using a drop shape analyzer equipment, see experimental procedure in Section 3.3.4. We have acquired series of three images for every interface, determined the contact angle from each one of them, and then performed their average to infer the results in Table 6.2. See Figure 6.5 for a representative image of each system. Note that the wettability of chloroform with Al_2O_3, $BiFeO_3$ and Si is virtually total, hence the value of θ cannot be accurately calculated - indicated as < 10º in Table 6.2, in subsequent calculations it has been assumed that $\theta = 0$º. We observe that the angle measured with water is less on UV-ozone surfaces, this being consistent with the expected increase in polarity of UV-ozone treated samples. Otherwise, PDMS has higher contact angles than those of other surfaces, and the fact that its θ values with water are very high (> 90º) indicates that it is a hydrophobic surface [121].

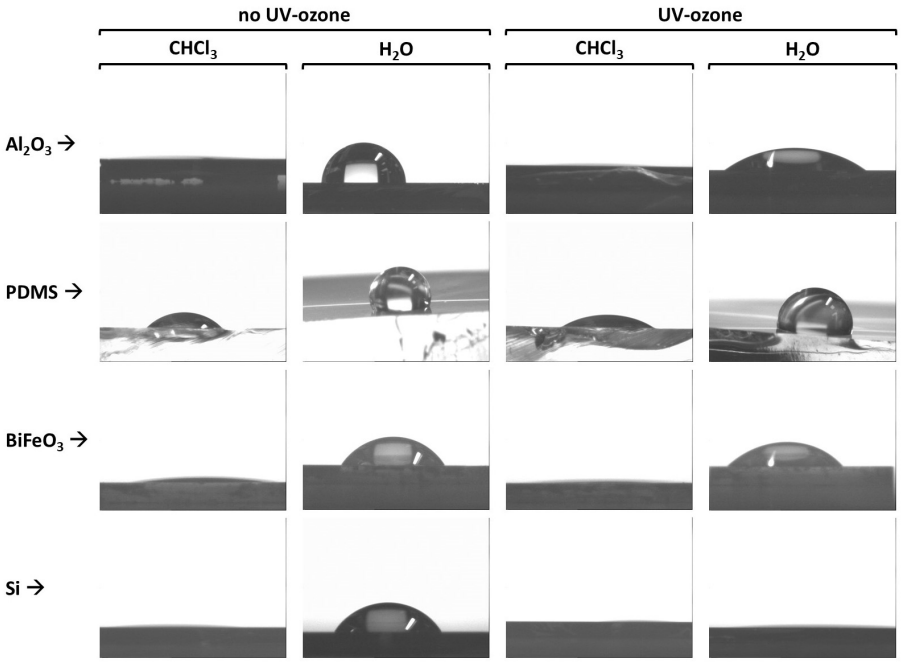

Figure 6.5: Photos of the solid-liquid interfaces: Al_2O_3, PDMS, $BiFeO_3$ and Si with chloroform and Milli-Q water (acquired with the drop shape analyzer equipment).

Secondly, we compute the SFE of Al_2O_3, $BiFeO_3$, PDMS and Si by applying the Fowkes model, which provides a simple procedure to determine the surface energy only using two properly selected solvents, in our case H_2O and chloroform. Accordingly, we need to solve the system of Equations 18, where γ_s^D and γ_s^P are the two unknown variables, θ is measured experimentally (see Table 6.2) and $\gamma_{l,i}^P$ are the surface tensions of each solvent (dispersive

and polar components), see Table 6.3.

Table 6.2: Contact angles of Al_2O_3, PDMS, $BiFeO_3$ and Si with water and chloroform

Contact angle (º)				
Solvent	no UV-O_3		UV-O_3	
	Al_2O_3	PDMS	Al_2O_3	PDMS
Water	87 ± 1	115 ± 4	40 ± 3	111 ± 4
Chloroform	< 10	45 ± 2	< 10	34 ± 3
	$BiFeO_3$	Si	$BiFeO_3$	Si
Water	57 ± 4	57.8 ± 0.2	47 ± 4	< 10
Chloroform	< 10	< 10	< 10	< 10

Table 6.3: Surface tensions of water and chloroform at 20ºC [13]

Solvent	Surface tension (mN/m)	Dispersive comp.	Polar comp.
Water	72.8	21.8	51.0
Chloroform	27.2	27.2	0

Since chloroform has γ_l^P = 0, we have determined γ_s^D of each solid with Equation 19, while γ_s^P has been computed with Equation 18, the results can be observed in Table 6.4. We note that the UV-ozone treatment makes the Al_2O_3, $BiFeO_3$ and Si samples more polar, considerably increasing the value of γ_s^P (by more than 3 times in Al_2O_3). It is noteworthy that the γ_s value of the two oxides is practically the same when they are UV-ozone treated, and Si has the highest SFE. On the other hand, PDMS does not show significant SFE differences, either with or without UV-ozone. Also, we see that the PDMS' γ_s has a very similar value to that we have previously estimated from extrapolating data of polymer melt (18 mN/m). Discrepancies are probably due to small differences in environmental conditions (temperature, relative humidity) during the acquisition of the experimental data. Besides, calculation from the parachor does not take into account variations due to a specific cross-linker:prepolymer ratio, [10:1] in our case.

Table 6.4: SFE of Al_2O_3, PDMS, $BiFeO_3$ and Si, with and without UV-ozone treatment, obtained from the contact angles measured before. * We assume $\theta = 0$º, no experimental error assigned.

Surface	SFE (mN/m)	Dispersive comp.	Polar comp.
Al_2O_3 (no UV-O_3)	22 ± 3	14*	9 ± 3
Al_2O_3 (UV-O_3)	57 ± 4	14*	44 ± 4
PDMS (no UV-O_3)	11 ± 3	10 ± 2	1 ± 2
PDMS (UV-O_3)	13 ± 3	11 ± 1	1 ± 1
$BiFeO_3$ (no UV-O_3)	43 ± 5	14*	30 ± 5
$BiFeO_3$ (UV-O_3)	52 ± 5	14*	38 ± 5
Si (no UV-O_3)	43 ± 5	14*	29 ± 5
Si (UV-O_3)	74*	14*	61*

Finally, Equations 21 and 24 have been used to determine W_{adh} of the Al_2O_3-PDMS, Al_2O_3-Si, $BiFeO_3$-PDMS and $BiFeO_3$-Si systems, for cases where the interface is exposed to the air and immersed in water, respectively, see Table 6.5. Notice that the more polar surfaces are, i.e. treated with UV-ozone, W_{adh} is much lower when the system is in an essentially polar media, such as water (0 mN/m in systems where Si is involved). On the other hand, when the environment is air, the adhesion is significantly higher (up to 130 mN/m in the Al_2O_3-Si system). In general, the difference in W_{adh} between exposing the sample to air or immersing it in water is much more important when they are treated with UV-ozone.

Table 6.5: Work of adhesion of the PDMS/oxide/Si interfaces.

W_{adh} (mN/m)				
no UV-ozone	PDMS		Si	
	Air	Water	Air	Water
Al_2O_3	31 ± 4	40 ± 5	62 ± 6	15 ± 3
$BiFeO_3$	44 ± 6	20 ± 5	86 ± 7	8 ± 2

UV-ozone	PDMS		Si	
	Air	Water	Air	Water
Al_2O_3	53 ± 6	10 ± 4	130 ± 4	0 ± 1
$BiFeO_3$	51 ± 6	13 ± 4	124 ± 5	0 ± 1

To sum up, in order to successfully attach the free-standing Al_2O_3 (or $BiFeO_3$) to PDMS, it is convenient to subject them to UV-ozone, thus increasing their SFE and the W_{adh} of the interface. Moreover, the joining of both surfaces should be performed in the air, allowing to achieve a stronger adhesion (53 vs 10 mN/m when Al_2O_3-PDMS system is immersed in water). Likewise, in order to transfer any of these oxide systems to Si, the incorporation of the new substrate should also be performed with the interface exposed to air, since in this case the W_{adh} of the oxide-Si system is higher than that of the oxide-PDMS system, and thus the transfer can be carried out successfully. Otherwise, Al_2O_3 or $BiFeO_3$ unhooking from PDMS is not favored, thus, relocating the active phase to Si will not be favored either.

In conclusion, we identify that this preliminary theroetical studies is an invaluable tool to optimize the procedure to manipulate and transfer free-standing oxides. In the case of free-standing Al_2O_3 and $BiFeO_3$, we have developed a protocol to explore oxide transfer from a polymer to Si substrate, including the optimal conditions to perform such operation and the most suitable surface treatments to achieve it successfully.

7 Conclusions

This project has demonstrated for the first time the viability of CSD to prepare $Sr_3Al_2O_6$ thin films, grown on $SrTiO_3$. We have shown that they are highly crystalline, epitaxial and pure-phase. In particular, we have reported that nitrate precursor solutions are distinctly stable, leading to homogeneous films with smooth surface morphology. Also, STEM cross-section images have revealed that a highly crystalline order is successfully achieved. In addition, we have proved that water is a reliable solvent to remove $Sr_3Al_2O_6$ films, placing this material as an effectively green and low-cost opportunity to produce sacrificial layers for water-resistant free-standing oxide manufacturing.

Secondly, we have shown that CSD-$BiFeO_3$ deposition on $Sr_3Al_2O_6$ gives rise to a nanocomposite material, where Sr and Al-rich square-shaped nanoparticles appear inside a $BiFeO_3$-rich matrix. Interestingly, both particles and matrix are shown to be crystalline phases.

On the other hand, we have proved that ALD is an attractive deposition technique to produce Al_2O_3/CSD-$Sr_3Al_2O_6$//$SrTiO_3$ heterostructures. Furthermore, we have developed a procedure to selectively remove $Sr_3Al_2O_6$ sacrificial layers by water etching in order to exfoliate Al_2O_3 thin films prepared by ALD, thus showing that this low-temperature deposition technique is an attractive candidate to synthesize free-standing oxides. Likewise, we have satisfactorily transferred the oxide film to PDMS.

We have performed a theoretical study on interfacial energy and polymer adhesion to investigate the principles of a successful free-standing oxide transfer to a hypothetical device substrate. It is shown that the work of adhesion (W_{adh}) allows to characterize the adherence between two solid surfaces as a quality strictly dependent on interfacial properties, which can be computed by contact angle measurements applying the Zisman model, Fowkes model or using equations of state. Hence, this theory provides a fundamental criterion to appropriately select surfaces and supports to manipulate free-standing oxides. In particular, we have stated that a successful transfer between substrates is feasible as long as the work of adhesion with the first substrate is lower than that with the second. All in all, this study on surface effects and adhesion is expected to be an invaluable tool to optimize procedures involving interfaces

For instance, in order to estimate under what conditions is the transfer of an oxide (Al_2O_3 or $BiFeO_3$) to Si favorable, we have determined the work of adhesion of the interfaces implicated in the procedure. Besides, we have explored the effect of different surface treatments (bare surface, UV-ozone) and environments (air, water). Accordingly, we have performed contact angle measurements with Milli-Q water and chloroform, and then we have computed the surface free energy of each material, and the W_{adh} of the oxide/substrate systems. As a result, we have demonstrated that relocation of an oxide thin film from PDMS to Si is theoretically favorable if the surfaces involved are UV-ozone treated, and the transfer

process is carried out in air exposure.

Overall, this project shows that nanoengineering techniques such as selective wet-etching and mechanical exfoliation could offer a viable platform to develop low-cost, versatile and scalable methods to peel-off and manipulate nanostructured free-standing layers, opening the door to their implementation into a wide spectrum of novel applications, including flexible photovoltaics.

There is still a long way to develop and perfect this promising novel free-standing technology. As a future work it is planned to conduct a further detailed microstructure study of the $Sr_3Al_2O_6$ thin films. Exfoliation and transfer procedures will also be improved by applying the principles of surface energy and interfacial adhesion here presented, selectively choosing the most suitable surface to capture and manipulate the complex oxide film. Furthermore, deposition of $BiFeO_3$ by low temperature ALD will be thoroughly studied, thereby progressing towards the manufacture of the first ferroelectric perovskite free-standing oxide prepared by low-cost chemical techniques.

Abbreviations Glossary

AFM: Atomic Force Microscopy

ALD: Atomic Layer Deposition

BFO: $BiFeO_3$

DSC: Differential Scanning Calorimetry

DTG: Derivative Thermogravimetry

CSD: Chemical Solution Depostion

EDX: Energy Dispersive X-Ray spectroscopy

FEPO: Ferroelectric Perovskite Oxides

FIB: Focused Ion Beam

HAADF: High-Angle Annular Dark-Field

MBE: Molecular Beam Epitaxy

MO: Metalorganic

N: Nitrate

PDMS: Polydimethylsiloxane

PLD: Pulsed Laser Deposition

PMMA: Poly(methyl methacrylate)

PV: Photovoltaic

RE: Rare Earth

SAO: $Sr_3Al_2O_6$

SEM: Scanning Electron Microscopy

SFE: Surface Free Energy

STEM: Scanning Transmission Electron Microscopy

STO: $SrTiO_3$

TGA: Thermogravimetric Analysis

TMA: Trimethylaluminium

UV-O_3: Ultraviolet light - Ozone

XRD: X-Ray Diffraction

References

[1] Ministerio para la Transición Ecológica y el Reto Demográfico. Spain. *Borrador Actualizado del Plan Nacional Integrado de Energía y Clima 2021-2030*. January 2020.

[2] Ji D. Cai S. et al. Freestanding crystalline oxide perovskites down to the monolayer limit. *Nature*, 560:87–90, 2019.

[3] Tilli M. Motooka T. et al. *Handbook of Silicon Based MEMS Materials and Technologies*. William Andrew, 2015. ISBN: 978-0-323-29965-7.

[4] Moshe H. Mastai Y. Atomic layer deposition on self-assembled-monolayers, 2012. DOI: 10.5772/54814.

[5] Component Parts of an XRD Diffractometer, 2016. URL: xrd.co/component-parts-x-ray-diffractometer.

[6] Jeol Ltd. high-angle annular dark-field scanning transmission electron microscopy, 2020. URL: jeol.co.jp/en/words/emterms.

[7] Bandyopadhyay A. Bose S. *Characterization of Biomaterials*. Elsevier, 2018. ISBN: 978-0-12-415800-9.

[8] Alonso Frank M. *Functionalization of Steels and other Metallic Materials with Hydrophobic Layers - Influence on Wetting and Corrosion Resistance*. PhD thesis, Friedrich–Alexander University Erlangen–Nürnberg, 2017.

[9] Bracco G. Holst B. *Surface Science Techniques*. Springer-Verlag Berlin Heidelberg, 2013. ISBN: 978-3-642-34243-1.

[10] University of Sheffield in collaboration with Ossila Ltd. Emma Spooner. A Guide to Surface Energy, 2020. URL: ossila.com/pages/a-guide-to-surface-energy.

[11] Quayle O.R. The Parachors of Organic Compounds. An Interpretation and Catalogue. *Chemical Reviews*, 53(3):439–589, 1953.

[12] Balasubrahmanyam S.N. Einstein, 'parachor' and molecular volume: Some history and a suggestion. *Current Science*, 94(12):1650–1658, 2008.

[13] van Oss C.J. *Interfacial Forces in Aqueous Media*. CRC Press, 2006. ISBN: 9780429134418.

[14] Coll M. Fontcuberta J. et al. Towards oxide electronics: a roadmap. *Applied Surface Science*, 482:1–93, 2019.

[15] Alexe M. Hesse D. et al. Tip-enhanced photovoltaic effects in bismuth ferrite. *Nature Communications*, 2(1):256–260, 2011.

[16] Machado P. Scigaj M. et al. Band gap tuning of solution-processed ferroelectric perovskite $BiFe_{1-x}Co_xO_3$ thin films. *Chemistry of Materials*, 31:947−954, 2019.

[17] Seyfouri M.M. Wang D. et al. Recent progress in bismuth ferrite-based thin films as a promising photovoltaic material. *Critical Reviews in Solid State and Materials Sciences*, 2020.

[18] Gu K. Katayama T. Simple method to obtain large-size single-crystalline oxide sheets. *Advanced Functional Materials*, 30(28):2001236, 2020.

[19] Zhang J. Coll M. et al. Electrodeposited Ni-based magnetic mesoporous films as smart surfaces for atomic layer deposition: an “all-chemical” deposition approach toward 3D nanoengineered composite layers. *ACS Applied Materials Interfaces*, 10(17):14877–14885, 2018.

[20] Stephen Cass. Solar power will make a difference–eventually, 2009. URL: technology review.com/2009/08/18/210913/solar-power-will-make-a-difference-eventually/.

[21] NREL National Renewable Energy Laboratory. Reserach cell record efficiency chart, 2020. URL: nrel.gov/pv.

[22] Battaglia C. Cuevas A. De Wolf S. High-efficiency crystalline silicon solar cells: status and perspectives. *Energy Environmental Science*, 9:1552–1576, 2016.

[23] Bisquert J. *The Physics of Solar Energy Conversion*. CRC Press, 2020. ISBN: 9781138584648.

[24] Yuan Y. et al. Arising applications of ferroelectric materials in photovoltaic devices. *Journal of Materials Chemistry A*, 2:6027–6041, 2014.

[25] Shockley W. Queisser H.J. Detailed Balance Limit of Efficiency of p□n Junction Solar Cells. *Journal of Applied Physics*, 32(3):510–519, 1961.

[26] Rühle S. Tabulated values of the Shockley–Queisser limit for single junction solar cells. *Solar Energy*, 130:139–147, 2016.

[27] Coll M. Fontcuberta J. et al. Towards Oxide Electronics: A Roadmap. *Applied Surface Science*, 482:1–93, 2019.

[28] Grinberg I. Vicent West D. et al. Perovskite oxides for visible-light-absorbing ferroelectric and photovoltaic materials. *Nature*, 503:509–512, 2013.

[29] Paillard C. Bai X. et al. Photovoltaics with ferroelectrics: current status and beyond. *Advanced Materials*, 28(26):5153–5168, 2016.

[30] Yang S.Y. Seidel J. et al. Above-bandgap voltages from ferroelectric photovoltaic devices. *Nature Nanotechnology*, 5:143–147, 2010.

[31] Fridkin V.M. Bulk photovoltaic effect in noncentrosymmetric crystals. *Crystallography Reports*, 26(4):654–658, 2001.

[32] Yang M. Lue Z. et al. Bulk photovoltaic effect in monodomain $BiFeO_3$ thin films. *Applied Physics Letters*, 110:183902, 2017.

[33] Yang M. Bhatnagar A. Alexe M. Electronic origin and tailoring of photovoltaic effect in $BiFeO_3$ single crystals. *Advanced Electronic Materials*, 11(1):1500139, 2015.

[34] Lóper-Varo P. Bertoluzzi L. et al. Physical aspects of ferroelectric semiconductors for photovoltaic solar energy conversion. *Physics Reports*, 653:1–40, 2016.

[35] Spanier J.E. Fridkin V.M. et al. Power conversion efficiency exceeding the Shockley–Queisser limit in a ferroelectric insulator. *Nature Photonics*, 10:611–616, 2016.

[36] Zhang F. Zhu K. Additive engineering for efficient and stable perovskite solar cells. *Advanced Energy Materials*, 10:1902579, 2020.

[37] Durruthy-Rodriguez M. Costa-Marrero J. et al. Photoluminescence in “hard” and “soft” ferroelectric ceramics. *Applied Physics A*, 98(3):434–550, 2010.

[38] Abd Razak N. Zabidi N. Rosli A. A first principle study of band structure of tetragonal barium titanate. *AIP Conference Proceedings*, 1875:020017, 2017.

[39] Yang Z. Rajagopal A. et al. Ideal bandgap organic–inorganic hybrid perovskite solar cells. *Advanced Materials*, 29(47):1704418, 2017.

[40] Yang S.Y. Martin L.W. et al. Photovoltaic effects in $BiFeO_3$. *Applied Physics Letters*, 95:062909, 2009.

[41] Ihlefeld J.F. Podraza N.J. et al. Optical band gap of $BiFeO_3$ grown by molecular-beam epitaxy. *Applied Physics Letters*, 92:142908, 2008.

[42] Singh S.K. Maruyama K. Ishiwara H. Reduced leakage current in La and Ni codoped $BiFeO_3$ thin films. *Applied Physics Letters*, 91(11):112913, 2007.

[43] Gupta S. Tomar M. et al. Ce-doped bismuth ferrite thin films with improved electrical and functional properties. *Journal of Materials Science*, 49(15):5355–5364, 2014.

[44] Schwarzkopf J. Fornari R. Epitaxial growth of ferroelectric oxide films. *Progress in Crystal Growth and Characterization of Materials*, 53(3):159–212, 2006.

[45] Kyun Lee S. Ho Choi B. Hesse D. Epitaxial growth of multiferroic $BiFeO_3$ thin films with (101) and (111) orientations on (100) Si substrates. *Applied Physics Letters*, 102:242906, 2013.

[46] Jiang Z. Guan Z. et al. Epitaxial growth of $BiFeO_3$ films on $SrRuO_3/SrTiO_3$. *Materials Characterization*, 131:217–223, 2017.

[47] Eres G. Tischler J.Z et al. *In Situ Characterization of Thin Film Growth*. Woodhead Publishing, 2011. ISBN: 978-1-84569-934-5.

[48] Zhang Y. Ma C. et al. Recent progress on flexible inorganic single-crystalline functional oxide films for advanced electronics. *Materials Horizons*, 6:911–930, 2019.

[49] Gao W. Zhu Y. et al. A review of flexible perovskite oxide ferroelectric films and their application. *Journal of Materiomics*, 6(1):1–16, 2020.

[50] Liu W. Wang H. et al. Flexible oxide epitaxial thin films for wearable electronics: fabrication, physical properties, and applications. *Journal of Materiomics*, 6(2):385–396, 2020.

[51] Kum H.S. Lee H. et al. Heterogeneous integration of single-crystalline complex-oxide membranes. *Nature*, 578:75–81, 2020.

[52] Lu D. Baek D.J. et al. Synthesis of freestanding single-crystal perovskite films and heterostructures by etching of sacrificial water-soluble layers. *Nature Materials*, 15:1255–1261, 2016.

[53] Bakaul S.R. Serrao C.R. et al. Single crystal functional oxides on silicon. *Nature Communications*, 7:10547, 2016.

[54] Bakaul S.R. Serrao C.R. et al. High speed epitaxial perovskite memory on flexible substrates. *Advanced Materials*, 29(11):1605699, 2017.

[55] Baek D.J. Lu D. et al. Ultrathin epitaxial barrier layer to avoid thermally induced phase transformation in oxide heterostructures. *Applied Materials and Interfaces*, 9(1):54–59, 2017.

[56] Baxamusa S.H. Stadermann M. et al. Enhanced delamination of ultrathin free-standing polymer films via self-limiting surface modification. *Langmuir*, 30(18):5126–5132, 2014.

[57] Sia W. Keten S. Size-dependent mechanical behavior of free-standing glassy polymer thin films. *Journal of Materials Research*, 30:36–45, 2015.

[58] Lange F.F. Chemical solution routes to single-crystal thin films. *Science*, 273(5277):903–909, 1996.

[59] Schwartz R.W. Schneller T. Waser R. Chemical solution deposition of electronic oxide films. *Comptes Rendus Chimie*, 7(5):433–461, 2004.

[60] Dorey R. et al. *Ceramic Thick Films for MEMS and Microdevices*. William Andrew, 2011. ISBN: 978-1-4377-7817-5.

[61] Schneller T. Waser R. et al. *Chemical Solution Deposition of Functional Oxide Thin Films*. Springer-Verlag Wien, 2013. ISBN: 978-3-7091-1915-0.

[62] Koster G. Huijben M. et al. *Epitaxial Growth of Complex Metal Oxides*. Woodhead Publishing, 2015. ISBN: 978-1-78242-245-7.

[63] Vila-Fungueiriño J.M. Rivas-Murias B. et al. Polymer assisted deposition of epitaxial oxide thin films. *Journal of Materials Chemistry C*, 6:3834–3844, 2018.

[64] Ohno T. Fujimoto M. Suzuki H. Preparation and characterization of PZT thin films on ITO/glass substrate by CSD. *Key Engineering Materials*, 301:41–44, 2006.

[65] Li Z. Coll M. et al. Control of nanostructure and pinning properties in solution deposited $YBa_2Cu_3O_7$−x nanocomposites with preformed perovskite nanoparticles. *Scientific Reports*, 9(5828), 2019.

[66] George S.M. Atomic Layer Deposition: an overview. *Chemical Reviews*, 110(1):111–131, 2010.

[67] Johnson R.W. Hultqvist A. Bent S.F. A brief review of atomic layer deposition: from fundamentals to applications. *Materials Today*, 17(5):236–246, 2014.

[68] Coll M. Napari M. et al. Atomic layer deposition of functional multicomponent oxides. *APL Materials*, 7:110901, 2019.

[69] Cochran E.A. Woods K.N. et al. Unique chemistries of metal-nitrate precursors to form metal-oxide thin films from solution: materials for electronic and energy applications. *Journal of Materials Chemistry A*, 7:24124–24149, 2019.

[70] Hartley Smith A.G. *Structural and Defect Properties of Strontium Titanate*. PhD thesis, University College London, Department of Chemistry, 2011.

[71] Sallés P. Caño I. et al. Solution processing of $Sr_3Al_2O_6$ for free-standing epitaxial complex oxides. *Paper in preparation*, 2020.

[72] Machado P. Preparation of novel nanoengineered ferroelectric oxide materials for photovoltaics. Master's thesis, ICMAB-CSIC (Barcelona), 2016.

[73] Kohli R. Mittal K.L. *Developments in Surface Contamination and Cleaning*. William Andrew, 2012. ISBN: 978-1-4377-7883-0.

[74] Zhou W. Wang Z.L. *Scanning Microscopy for Nanotechnology. Techniques and Applications*. Springer-Verlag New York, 2007. ISBN: 978-1-4419-2209-0.

[75] Hawkes P.W. Spence J.C.H. *Springer Handbook of Microscopy*. Springer, 2019. ISBN: 978-3-030-00069-1.

[76] Zhang J.Y. Hwang I. et al. Variable-angle high-angle annular dark-field imaging: application to three-dimensional dopant atom profiling. *Scientific Reports*, 5(12419), 2019.

[77] Treacy M.M.J. Z dependence of electron scattering by single atoms into annular dark-field detectors. *Cambridge University Press*, 17(6):847–858, 2011.

[78] Haugstad G. *Atomic Force Microscopy: Understanding Basic Modes and Advanced Applications*. Wiley, 2012. ISBN: 978-0-470-63882-8.

[79] Brune D. hellborg R. et al. *Surface Characterization: A User's Sourcebook*. Wiley, 2008. ISBN: 978-3-527-61244-4.

[80] Reimer L. *Scanning Electron Microscopy*. Springer-Verlag Berlin Heidelberg, 1998. ISBN: 978-3-540-63976-3.

[81] Nanakoudis A. SEM: Types of Electrons and the Information They Provide, 2019. URL: thermofisher.com/blog/microscopy/sem-types-electrons-and-the-information-they-provide.

[82] Ebnesajjad S. *Surface Treatment of Materials for Adhesive Bonding*. Elsevier, 2014. ISBN: 978-0-323-26435-8.

[83] Inczedy J. Lengyel T. Ure A.M. *IUPAC Compendium on Analytical Nomenclature, Definitive Rules*. William Andrew, 1997. ISBN: 0-632-05127-2.

[84] Wagner M. *Thermal Analysis in Practice*. Hanser, 2018. ISBN: 978-1-56990-643-9.

[85] Krüss Scientific. Drop Shape Analyzer - DSA100. Technical report, 2020.

[86] Zhang P. Xu M. et al. Synthesis and characterization of europium-doped $Sr_3Al_2O_6$ phosphors by sol–gel technique. *Journal of Sol-Gel Science and Technology*, 43:59–64, 2007.

[87] Melnikov P. Nascimento V.A. et al. Thermal decomposition mechanism of aluminum nitrate octahydrate and characterization of intermediate products by the technique of computerized modeling. *Journal of Thermal Analysis and Calorimetry*, 111:543–548, 2013.

[88] Wyrzykowski D. Hebanowska E. et al. Thermal behaviour of citric acid and isomeric aconitic acids. *Journal of Thermal Analysis and Calorimetry*, 104:731–735, 2011.

[89] Barbooti M.M. Al-Sammerrai D.A. et al. Thermal decomposition of citric acid. *Thermochimica Acta*, 98:119–126, 1986.

[90] Gallagher P.H. Thermal decomposition of strontium nitrite monohydrate. *Thermochimica Acta*, 75:121–127, 1984.

[91] Hoene J. Charles R.G. Hickam W.M. et al. Thermal decomposition of metal acetylacetonates mass spectrometer studies. *Journal of Physical Chemistry*, 62(9):1098–1101, 1958.

[92] Duan Y. Li J. et al. Thermal investigation of strontium acetate hemihydrate in nitrogen gas. *Journal of Thermal Analysis and Calorimetry*, 94(1):169–174, 2008.

[93] Langjahr P.A. Lange F.F. et al. Lattice mismatch accommodation in perovskite films on perovskite substrates. *Acta Materialia*, 46(3):773–785, 1998.

[94] Golovina I.S. Falmbigl M. et al. Effect of annealing conditions on the electrical properties of ALD-grown polycrystalline $BiFeO_3$ films. *Journal of Materials Chemistry C*, 6:5462–5472, 2018.

[95] Sigov A. Podgorny Yu. et al. Leakage currents in ferroelectric thin films. *Phase Transitions*, 86(11):1141–1151, 2013.

[96] Kim H. Yang S. et al. Leakage current analysis depends on grain size variation in zinc oxide thin film transistor . *CS Meeting Abstracts*, 71, 2013.

[97] Smith B.W. Suzuki K. *Microlithography: Science and Technology*. CRC Press, 2018. ISBN: 9781420051537.

[98] Ariel-Sternberg N. PMMA resist processing standard operating procedure. Technical report, Columbia Nano initiative - Center for Integrated Science and Engineering, Columbia University (New York).

[99] Her M. Beams R. Novotny L. et al. Graphene transfer with reduced residue. *Physics Letters A*, 377:1455–1458, 2013.

[100] Lu D. Crossley S. et al. Freestanding oxide ferroelectric tunnel junction memories transferred onto silicon. *Nano Letters*, 19:3999−4003, 2019.

[101] Jost M. Kagelman L. Monolithic perovskite tandem solar cells: a review of the present status and advanced characterization methods toward 30% efficiency. *Advanced Energy Materials*, page 1904102, 2020.

[102] Miyake S. *Novel Materials Processing by Advanced Electromagnetic Energy Sources*. Elsevier Science, 2005. ISBN: 978-0-08-044504-5.

[103] Young T. An essay on the cohesion of fluids. *Transactions of the Royal Society of London*, 95:65–87, 1805.

[104] Huhtamäki T. Tian X. et al. Surface-wetting characterization using contact-angle measurements. *Nature Protocols*, 13:1521–1538, 2018.

[105] Biolin Scientific. Attension Theory Note 4: Surface free energy - theory and calculations. Technical report, 2020.

[106] Zisman W.A. Relation of the equilibrium contact angle to liquid and solid constitution. *Advances in Chemistry*, 43:1–51, 1964.

[107] Zenkiewicz M. Methods for the calculation of surface free energy of solids. *Journal of Achievements in Materials and Manufacturing Engineering*, 24(1):137–145, 2007.

[108] Kwok D.Y. Neumann A.W. Contact angle measurement and contact angle interpretation. *Journal of Achievements in Materials and Manufacturing Engineering*, 81(3):167–249, 1999.

[109] Grifalco L.A. Good R.J. A theory for the estimation of surface and interfacial energies. I. Derivation and application to interfacial tension. *Journal of Physical Chemistry*, 61(7):904–909, 1957.

[110] Neumann A.W. Li D. A reformulation of the equation of state for interfacial tensions. *Journal of Colloid and Interface Science*, 137(1):304–307, 1990.

[111] Fowkes F.M. Attractive forces at interfaces. *Industrial Engineering Chemistry*, 56(12):40–52, 1964.

[112] Subedi D.P. Contact angle measurement for the surface characterization of solids. *The Himalayan Physics*, 2(2):1–4, 2011.

[113] Rulison C. Two-component surface energy characterization as a predictor of wettability and dispersibility. *Krüss Application Reports*, 213:1–13, 2000.

[114] Exner O. Conception and significance of the parachor. *Nature*, 196:890–891, 1962.

[115] Agrawal A. Surface Tension of Polymers, 2005. Department of Mechanical Engineering, Massachusets Institute of Technology (MIT).

[116] van Krevelen D.W. Nijenhuis K. *Properties of Polymers*. Elsevier Science, 2009. ISBN: 9780080915104.

[117] Polymer Properties Database. Poly(dimethylsiloxane), 2017. URL: polymer-database.com/polymers/Polydimethylsiloxane.html.

[118] American Chemical Society. Molecule of the Week Archive: Polydimethylsiloxane, 2014. URL: acs.org/content/acs/en/molecule-of-the-week/archive.

[119] Brandrup J. Immergut E.H. Grulke E.A. *Polymer Handbook*. Wiley-Interscience, 1999. ISBN: 0-471-16628-6.

[120] Ossila. Enabling materials science. UV Ozone Cleaner, 2020. URL: ossila.com/products/uv-ozone-cleaner.

[121] Law K. Definitions for hydrophilicity, hydrophobicity, and superhydrophobicity: getting the basics right. *Journal of Physical Chemistry Letters*, 5(4):686–688, 2014.